TEKTONIKA

Brittle-ductile Coupling and Block Rotation During Rifting Revealed Through Digital Volume Correlation Analysis of a Crustal-scale Analogue Experiment

Timothy C. Schmid *[1], **Jürgen Adam** [2], **Frank Zwaan** [1,3,4], **Guido Schreurs** [1], **Dave Hollis** [5]

[1]Institute of Geological Sciences, University of Bern, Switzerland | [2]Department of Earth Sciences, Royal Holloway University London, England | [3]Helmholtz Centre Potsdam – GFZ German Research Centre for Geosciences, Potsdam, Germany | [4]Department of Geosciences, University of Fribourg, Switzerland | [5]LaVision UK Ltd, England

Abstract During rifting, blocks of upper brittle crust may rotate about a vertical axis above the ductile parts of the crust below, in particular in settings where two rift segments interact in a so-called rift-pass structure, with important implications for our understanding of rift system development. However, whether such block rotation is edge-driven (induced by deformation in the brittle crust itself), or by viscous flow in the underlying ductile crust, and what role kinematic coupling between material in the brittle and ductile crust plays remains unclear. In this study, we apply new digital volume correlation (DVC) analysis on a previously presented crustal-scale analogue model simulating the evolution of a rift-pass structure. The improvements to our new DVC workflow include data preprocessing, increased vector resolution, improved postprocessing, and deformation quantification using finite stretch and rotation tensors. This enhanced workflow allows us to quantify the kinematic coupling between the brittle and viscous model layers in much higher spatial resolution, and to determine previously unrecognized differences in deformation styles between the brittle and viscous layers. Our improved DVC analysis reveals new insights into the kinematic evolution of a rotating rift-pass block forming between two interacting rift segments. We document (1) the evolution of a rift-pass block in the brittle layer, (2) its effect on the underlying viscous model layer and, (3) the kinematic coupling between the two model layers. Laterally confined by two rift segments, the rift-pass block rotates about a vertical axis and exerts a drag force on the underlying viscous layer where rift-axis parallel viscous flow is stimulated. As a result, a brittle-ductile transitional zone forms that shows increased shear with spatial and temporal variations in the degree of kinematic brittle-viscous coupling. Our DVC analysis suggests that edge-driven rift-pass block rotation locally weakens kinematic coupling, resulting in rift-axis parallel flow in the lower crust. Hence, rotating blocks in the upper crust may induce considerable amount of lower-crustal material to flow out of a 2D plane, which must be considered when estimating crustal extension from rift-axis perpendicular cross-sections.

Executive Editor:
Janine Kavanagh
Associate Editor:
L. Muniz Pichel
Technical Editor:
Mohamed Gouiza

Reviewers:
Taco Broerse
Jacqueline Reber

Submitted:
4 November 2022
Accepted:
6 August 2024
Published:
31 October 2024

1 Introduction

The linkage of individual rift segments is a fundamental aspect of a rift system on its way to continental breakup. In the past, various studies focused on step-over regions where such linkage occurs, as they represent areas of potential for hydrocarbon exploration (e.g., *Bosworth*, 1985; *Fossen et al.*, 2010; *Gawthorpe and Hurst*, 1993; *Morley et al.*, 1990; *Nelson et al.*, 1992; *Rosendahl*, 1987). Step-over linkage structures are the result of two (or more) individual laterally propagating rift segments (*Koehn et al.*, 2008). In the case of a large enough lateral offset, the two mutually propagating rift segments may overlap and turn toward each other resulting in a rift-pass structure (e.g., *Acocella*, 2008; *Glerum et al.*, 2020; *Morley et al.*, 1990; *Nelson et al.*, 1992; *Tentler and Acocella*, 2010; *Zwaan and Schreurs*, 2017, 2020; *Zwaan et al.*, 2016). Thereby, a rift-pass block (i.e., the central area confined by the propagating rifts; *Nelson et al.*, 1992) acts as a nearly non-deforming unit as strain is diverted along the confining rift segments (*Brune et al.*, 2017) and, due to the overlapping arrangement of the adjacent rift arms, may rotate about a vertical axis (*Glerum et al.*, 2020; *Oldenburg and Brune*, 1975; *Zwaan et al.*, 2016). Such rift-pass structures occur at various scales from micro-crack interaction (*Pollard and Aydin*, 1984) to lithosphere-scale continental microplates such

*✉ timothy.schmid@unibe.ch

as the Victoria microplate, that is bounded by the western and eastern branches of the East African Rift System (EARS; e.g., *Glerum et al.*, 2020 and references therein; *Nelson et al.*, 1992; Figure 6 in *Pollard and Aydin*, 1984; *Zwaan and Schreurs*, 2023).

In the continental lithosphere, blocks of the upper brittle crust resting on a viscous substratum (i.e., a lower crustal part that deforms in a ductile manner) may rotate about a vertical rotation axis. However, the role of the ductile lower crust in such settings was strongly debated in the 1980s to 2000s, without a clear resolution so far (*Axen et al.*, 1998; *Giorgis et al.*, 2004; *Jackson et al.*, 1992; *Jackson and Molnar*, 1990; *McKenzie and Jackson*, 1983, 1986; *Tikoff et al.*, 2004, 2002). If block rotation originates in the upper brittle crust (Figure 1a; i.e., edge-driven model; *Schouten et al.*, 1993), it exerts a basal shear stress on the lower crust perturbing the underlying viscous flow field (*Lachenbruch and Sass*, 1992; *Lamb*, 1994). In contrast, if the underlying viscous flow field controls rigid block rotation in the brittle upper crust (Figure 1b; i.e., floating block model; *McKenzie and Jackson*, 1983, 1986), displacements must be similar in both layers (*Lamb*, 1994). In the latter case, motions in the brittle upper and ductile lower crust are kinematically coupled, whereas in the former case a horizontal transitional layer between the two layers must be present with enhanced horizontal shearing that determines the degree to which motions at depth are coupled to near-surface movements (*Thatcher*, 1995). Multiple definitions of coupling of brittle and viscous layers are used in the literature (e.g., *Brun*, 1999; *Buck*, 1991; *Schueller et al.*, 2010; *Zwaan et al.*, 2019). Most definitions have in common that they describe coupling partly as a function of the viscous strength leading to different degrees of coupling over time. Here, we investigate spatial variations of coupling between the brittle and viscous model layers as expressed by spatially varying shear strains at the brittle-viscous interface.

Analogue and numerical models provide excellent tools to study the kinematic and dynamic evolution of rift-pass structures and the evolution of lithospheric microplates. However, many modelling studies focus on the brittle domain only (e.g., the brittle upper crust; *Acocella et al.*, 1999; *Allken et al.*, 2011; *Koehn et al.*, 2008; *Paul and Mitra*, 2012). Modelling studies that do include the ductile lower crust in the shape of a viscous layer often lack a detailed analysis of the viscous deformation (e.g., *Allken et al.*, 2012; *Zwaan and Schreurs*, 2017; *Zwaan et al.*, 2018, 2016) and to this date, little effort has been made to obtain a quantitative description of model deformation within the ductile lower crust, particularly in the context of rift-pass structures.

While numerical models provide the advantage of direct access to model parameters that give insights into rift kinematics (e.g., velocities, strain rates) and dynamics (e.g., pressure, stresses) analogue models require further measures to quantify deformation. Possibilities to quantify deformation range from manual analysis of passive marker displacements (e.g., *Schellart et al.*, 2003) to fully automatized algorithms tracking displacement- or velocity-derived entities (*Adam et al.*, 2005; *Boutelier*, 2016; *Boutelier et al.*, 2019; *Broerse et al.*, 2021; *Chaipornkaew et al.*, 2022; *Thielicke and Stamhuis*, 2014; *Toeneboehn et al.*, 2018). While such techniques, for example Digital Image Correlation (DIC), have become a common tool to quantify surface deformation, the use of opaque model materials poses a severe obstacle to document internal deformation in analogue models. This limits the use of image correlation techniques for quantitative deformation analysis to model surfaces and/or side view imagery through transparent sidewalls (e.g., *Adam et al.*, 2005). Alternatively, internal deformation may be accessible by cutting cross sections at the end of an experiment, but such procedures fail to capture the transient nature of deformation (e.g., *Dooley et al.*, 2009).

Volumetric imaging techniques such as X-ray computed tomography (XRCT; *Hounsfield*, 1973) applied on analogue model experiments overcome the aforementioned difficulties as it provides a non-destructive imaging technique that documents the model evolution (e.g., *Colletta et al.*, 1991; *Mandl*, 1988; *Panien et al.*, 2006; *Schreurs et al.*, 2003, 2002). Digital Volume Correlation (DVC) extends the principles of DIC for volumetric data sets (such as sequential XRCT scans acquired at different time steps during progressive deformation) and provides an outstanding opportunity to investigate and track deformation in otherwise opaque model materials in a quantitative manner (*Adam et al.*, 2013). Like DIC, DVC is based on the correlation of scalar intensities of volumetric pixels (i.e., voxels).

Adam et al. (2013) used DVC to investigate thrusting in the upper crust. Their model consisted of a purely brittle setup (i.e., quartz sand) placed on a rigid base with a basal velocity discontinuity to initiate a pop-up structure confined by two conjugate thrust faults (shear zones). A recent crustal-scale analogue modelling study by *Zwaan et al.* (2018) investigated how rift interaction structures develop in different tectonic settings and how syn-rift sedimentation affects first-order structures of rift segment evolution. To this end, they applied DVC on crustal-scale brittle-viscous analogue experiments to study model internal viscous deformation in subsequent XRCT scans and quantified the rise of viscous material below rift basins. *Poppe et al.* (2019) made use of DVC on wide beam XRCT imagery volumes to quantify kinematics and dynamics of magmas intruding into a host rock (i.e., syrup intrusions into a granular sand-plaster mixture). More recently, *Schmid et al.* (2022) investigated the role of lower crustal flow in continental extension under the influence of an along-axis divergence-velocity gradient (i.e., rotational rifting; *Martin*, 1984; *Zwaan et al.*, 2020). *Schmid et al.* (2022) documented substantial rift-axis parallel

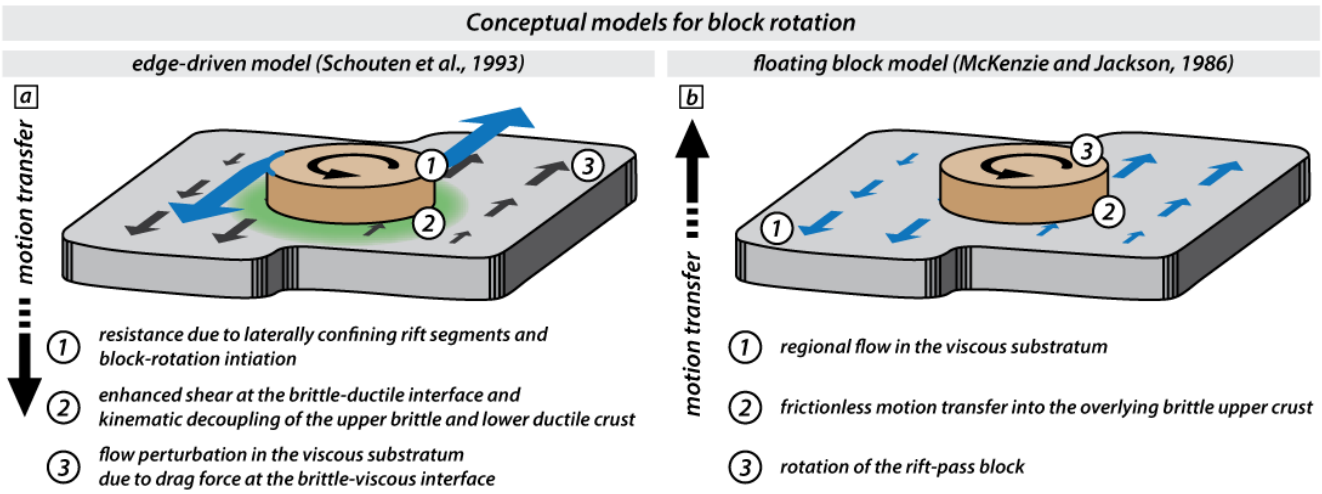

Figure 1 – Conceptual models of rift-pass block rotation about a vertical axis. **a)** Edge-driven model (*Schouten et al.*, 1993) for block rotation in the upper brittle crust. The rift-pass block rotates driven by interactions on its lateral margins, where considerable resistance occurs (blue arrows) along the confining rift segments. The upper-crustal-driven rotation causes a horizontal transitional layer (green shade) with enhanced shear below the brittle crust and exerts a drag force on the underlying viscous substratum where flow occurs. **b)** Floating block model (*McKenzie and Jackson*, 1986). Rotation of the rift-pass block in the upper brittle crust is driven by a deforming continuum (i.e., viscous flow) beneath the brittle crust with negligible resistance on the lateral margins of the rift-pass block.

flow towards zones of higher total extension. They described kinematic coupling processes between brittle upper and viscous lower crustal parts in a quantitative manner and concluded that, in such settings, rift-axis parallel flow can eventually exert a drag force on the brittle upper crustal material that sits on top of the viscous model layer.

The high costs of maintaining and operating XRCT scanners poses a severe restriction for more detailed analysis of model internal deformation exemplified by the scarce number of existing DVC studies. Thus, analogue modelers should consider revisiting existing XRCT data sets for DVC analysis to gain new quantitative insights. However, there are important considerations to keep in mind when performing DVC on existing data sets: for example, successful DVC analysis depends on the quality of the underlying XRCT data and improperly scaled XRCT data sets may lead to misinterpretation of displacements in the model. Moreover, meaningful improvements to previous interpretations of DVC results may require further postprocessing of the data and the selection of appropriate strain tensors for investigating the kinematics of tectonic processes.

In this study, we apply a new DVC workflow (including XRCT preprocessing, increased vector resolution, DVC postprocessing and appropriate use of strain quantities) on a crustal-scale analogue model simulating the evolution of a rift-pass structure from *Zwaan et al.* (2018). With the use of this new DVC workflow, we investigate the evolution of the aforementioned rift-pass structure and its effect on lower crustal deformation by studying the degree of kinematic coupling between the brittle and viscous model layers. Our results give new and more detailed insights into the evolution of a rift-pass structure and concomitant stimulation of rift-axis parallel lower-crustal flow that may occur in natural rift-pass structures. We show that such rift-axis parallel lower-crustal flow may transport a substantial amount of material out of a 2D section plane resulting in overestimation of crustal extension in rift sections if not taking into account the full 3D flow.

2 Methods

2.1 General Model Set-up

The model from *Zwaan et al.* (2018) that we re-analyze for this study represents a rift-pass structure developing in a brittle-ductile crust with radiogenic heat production on top of a viscously deforming weak mantle. In such settings, the strength of the lithosphere is determined by the brittle upper crust (e.g., *Bürgmann and Dresen*, 2008; *Mareschal and Jaupart*, 2013; *Zwaan et al.*, 2019), and the rift-pass develops due to reactivation of an offset-inherited weakness in the upper crust during rifting.

The model setup involves a compressible base consisting of a set of alternating plexiglass and foam bars (0.5 cm and 1 cm wide, respectively, totaling 36.5 cm) that is compressed to a width of 30 cm prior to the model build-up (Figure 2a, b). This specific setup was needed for other experiments in *Zwaan et al.* (2018) simulating oblique rifting; however, a strike-slip component of motion was not applied in the orthogonal rifting model presented here. On top of this base, a 4 cm thick lower viscous layer and a 4 cm thick upper brittle layer are inserted, simulating a thick lower ductile crust due to radiogenic heating, and a relatively

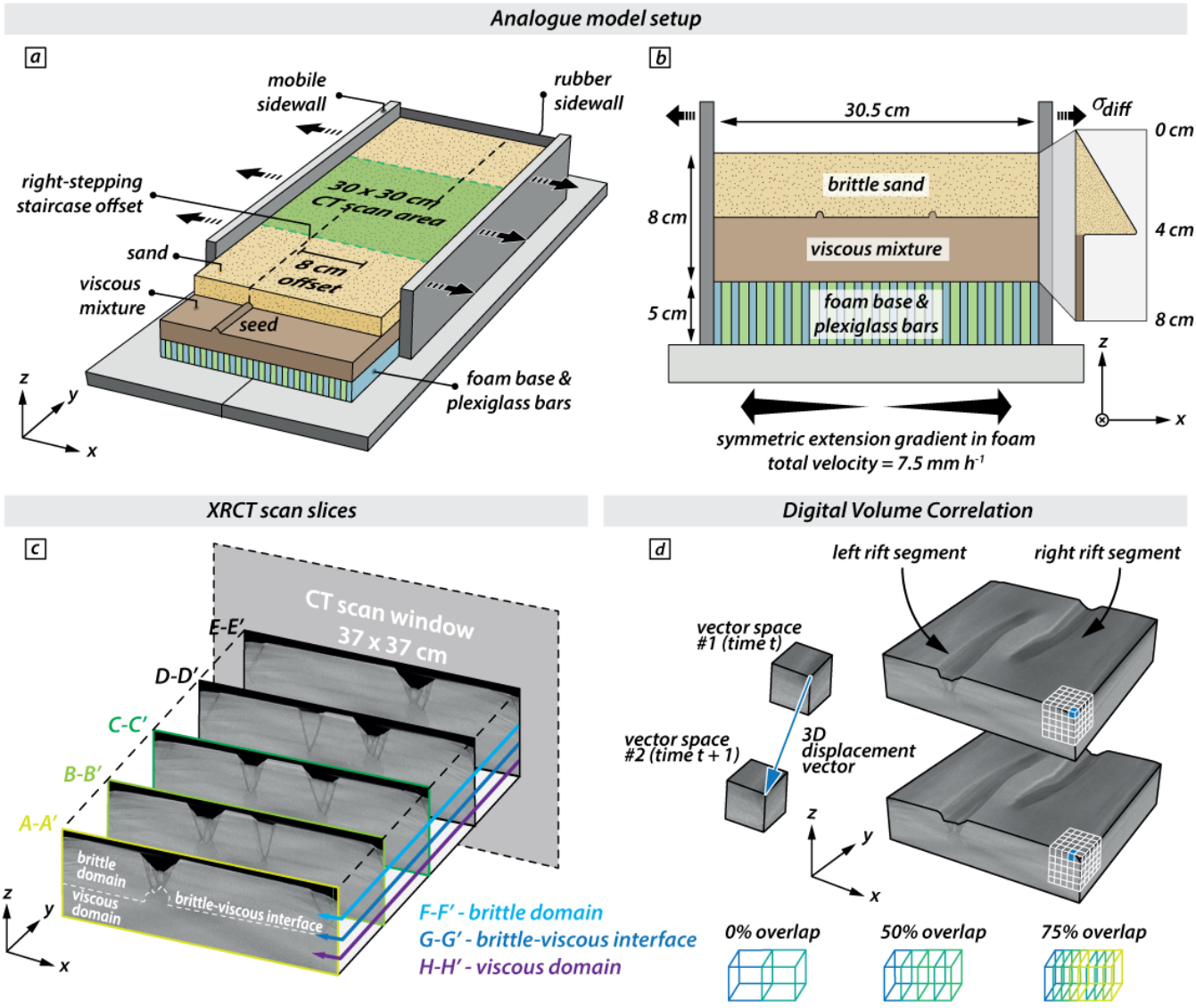

Figure 2 – Model setup and positions of XRCT slices. **a)** Cut-out view of the experimental apparatus. The model is confined by two mobile sidewalls and sits on top of a basal foam-plexiglass setup. The model is confined at the short side walls by two rubber side walls (only one visible here). Black arrows refer to the applied divergence direction. See text for details. **b)** The model setup consists of a brittle sand layer representing the upper brittle crust on top of a viscous mixture of PDMS and corundum sand imitating the lower ductile crust. The two-layer model sits on top of a basal foam-plexiglass setup extending homogeneously after compression before the experiment run. The total velocity refers to the motion of the side walls and the outermost parts of the basal setup. Black arrows refer to the applied divergence direction. **c)** Distinct XRCT slices of the XRCT volume that indicate positions of the analyzed model transects. A-A' – outermost transect; B-B' – intermediate rift transect; C-C' – central transect. D-D' and E-E' – intermediate and outermost transects, respectively, on the opposite model domain. F-F', G-G', and H-H' refer to horizontal slices in the center of the brittle layer, at the brittle-viscous interface, and in the center of the viscous layer, respectively. The grey window indicates the initial size of the XRCT scan window of 37 x 37 cm. **d)** Digital Volume Correlation applied on two subsequent XRCT volumes. The data volume is divided into smaller interrogation volumes, consisting of a cubic set of voxels, to determine local displacement vectors by identifying similar intensity patterns in subsequent time-series volume data sets.

thin upper brittle crust, respectively (*Zwaan et al.*, 2019). Semi-cylindrical Seeds (PDMS/corundum sand mixture rods with a radius of ca. 0.5 cm) inserted on top of the viscous layer allow the localization of rifting in the brittle layer (Figure 2a, b). Above these seeds, the sand locally thins, reducing the brittle strength and resulting in faulting and rift basin formation (Figure 2b). Generally, such seeds act as pre-existing weak zones along which deformation initiates (e.g., *Collanega et al.*, 2018; *Heilman et al.*, 2019; *Kolawole et al.*, 2018; *Le Calvez and Vendeville*, 2002). Note that, hereafter, we refer to the developing rift branches above these seeds as the left (i.e., negative x-axis values) and right (i.e., positive x-axis values) segment (Figure 2d).

After applying the brittle and viscous model materials, high-precision computer-controlled motors move the mobile sidewalls outward, providing a symmetric (with respect to the x-axis) velocity boundary condition as the base of the

model expands in a uniform manner, representing the deformation of a ductile lithospheric mantle (Figure 2b). At its short ends, the model is confined by rubber sidewalls that stretch uniformly as the mobile sidewalls move apart over the course of the experiment (Figure 2a). This uniform stretching differs from the rigid block-style deformation of the brittle layer, potentially causing minor boundary effects along the short ends of the model, which however do not impact our analysis that is focused on the center of the model (Figure 2a). All components of the machine surrounding the model are built of X-ray transparent materials that allow for XRCT-scanning (see Section 2.2). The divergence velocity is set relatively low at 7.5 mm h^{-1} to avoid high degrees of brittle-viscous coupling and the resulting distributed deformation (i.e., wide rifting) in the brittle sand layer (e.g., *Brun*, 1999; *Buiter et al.*, 2008; *Zwaan et al.*, 2016). With the applied divergence velocity field, faulting in the brittle layer strongly localizes above the seeds, although some boundary effects still occur along the longitudinal sidewalls (see Supporting Information SI-1 and SI-2 and *Zwaan et al.*, 2018 for details). The divergence velocity field and its orthogonal direction (with respect to the seeds) are kept constant for the duration of the model run, resulting in 30 mm widening or a total strain of ca. 10%, given a model run of 4 h and the initial 30.5 cm model width.

For the viscous layer, *Zwaan et al.* (2018) use a mixture of polydimethylsiloxane (PDMS) and corundum sand to achieve the required density, whereas the brittle layer consists of quartz sand (see Supporting Information SI-1 and *Zwaan et al.*, 2018 for material properties). Both modelling materials are mixed with high-density Zirshot ceramic microbeads (weight ratio 1:50) to enhance volumetric patterns on XRCT scans, thus facilitating the correlation of intensity patterns in the subsequent DVC analysis. The experiment we re-analyze involves a disconnected, right-stepping "staircase offset" seed geometry (angle φ of 90° i.e., no seed under- or overlap; Figure 2a) with a seed offset of 8 cm (see also *Zwaan et al.*, 2018, Figure 2h for details).

2.2 X-ray CT Data Acquisition

The internal deformation of the model is captured using a 64-slice Siemens Somatom Definition AS medical XRCT scanner. XRCT-scanning represents a unique, non-destructive method for detailed (sub-mm scale) 3D analysis of the model surface and internal structural evolution. This technique relies on attenuation contrasts (i.e., mainly density variations in the model), which show up as different intensities on the XRCT images (e.g., *Colletta et al.*, 1991; *Schreurs and Colletta*, 1998; *Schreurs et al.*, 2003). Faults, or rather shear zones, become visible in XRCT images because the sand experiences a local density reduction due to sand dilation as sand grains move past each other (*Panien et al.*, 2006, and references therein).

For XRCT data acquisition, the experiment from *Zwaan et al.* (2018) is scanned at regular timesteps with a 20-minute interval (corresponding to 2.5 mm extension increments). During each time step, the applied divergence velocity is halted and the model is scanned 5 times to acquire multiple XRCT data sets for all 13 timesteps (including t = 0 and considering a model run of 240 min). The duration of these interruption periods is kept at a minimum to avoid ongoing deformation in the time-dependent viscous layer. Stacking of all 5 XRCT data sets per timestep increases the volumetric intensity patterns and the signal-to-noise ratio, facilitating the subsequent DVC analysis (*Adam et al.*, 2013). As the applied scan protocol is resource intensive and may cause overheating, XRCT-scanning is performed on a reduced horizontal scan area of 30 x 30 cm in the center of the experiment (Figure 2a, c, d).

An iterative reconstruction kernel optimized for bone tissue (i.e., I70f for high density materials), which allows the best visualization of internal features in the model materials, is used to export the XRCT data set to the industry standard DICOM file format. Medical software (HOROS for MacOS) allows full 3D examination of the XRCT data and (internal) model structures. In the XRCT plane (i.e., the xz-plane; Figure 2c), the matrix resolution is 512 x 512 pixels for each slice with a scan window of 370 x 370 mm, resulting in an effective resolution of 0.72 x 0.72 mm/px. Perpendicular to the XRCT scanning plane (i.e., along the y-axis), each XRCT scan slice has a thickness of 0.6 mm (i.e., effective resolution of 0.6 mm/px) with a slice increment of 0.3 mm (thus, 0.3 mm slice overlap). This yields volumetric pixels (voxels) with dimensions of 0.72 x 0.6 x 0.72 mm/px (x-, y-, and z-axis; see Figure 2).

2.3 Revised Digital Volume Correlation Analysis

The improvements in our new DVC workflow, with respect to the original *Zwaan et al.* (2018) study, include better data preprocessing, increased vector resolution, improved postprocessing, and deformation quantification using finite stretches and rotations. This enhanced workflow allows us to quantify the kinematic coupling between the brittle and viscous model layers in much higher spatial resolution, and to determine previously unrecognized differences in deformation styles between the brittle and viscous layers.

In principle, DVC computes 3D displacement fields by cross-correlating intensity patterns from subsequent volumetric (XRCT scanned) data sets in a time series (*Adam et al.*, 2013; *Poppe et al.*, 2019; *Schmid et al.*, 2022; *Zwaan et al.*, 2018). The data volume is divided into small interrogation volumes (i.e., sub-volumes) consisting of a cubic set of multiple voxels to determine local displacement vectors (per sub-volume) by cross-correlating identical intensity patterns in subsequent time-series volume data

sets (Figure 2d). By moving the interrogation sub-volume over a part of the data volume with defined search radius, correlation values in the range [0, 1] are represented by a spherical blob in 3D. For each sub-volume, the best matching position is represented by a correlation peak and is associated with the displacement vector components u_x, u_y, and u_z in reference to the deformed volume. As each individual sub-volume yields one local displacement vector, the resulting incremental displacement field consists of all 3D vectors of all sub-volumes. The resulting vector resolution depends on the size of the interrogation sub-volume and individual voxel size. Smaller interrogation sub-volumes may capture smaller inhomogeneities in the deformation (e.g., shear zones); however, they are also more sensitive to random noise than larger interrogation sub-volumes (*Wieneke*, 2017).

We use the commercial DaVis software (version 10.2, from LaVision) to perform a multi-pass DVC analysis. DaVis first uses a computationally efficient Fast Fourier Transform (FFT) algorithm in the spectral domain that computes the correlation map for the entire volume data and defines an initial predictor displacement vector. Subsequent iterations use a direct correlation (DC) algorithm in the spatial domain on successively smaller sub-volumes and successively smaller search radii. In the resulting displacement vector field, the number of vectors is identical to the number of sub-volumes in the entire volume. However, shifting the interrogation sub-volume by a small distance, smaller than the sub-volume edge length, results in a higher vector density as the sub-volumes for which the correlation is calculated overlap (Figure 2d). Note that, the overlap of sub-volumes does not improve the spatial resolution as neighboring vectors are not independent; however, it increases vector resolution leading to smoother results and less discontinuities. Since the subsequent DVC analysis requires cubic voxels with the same edge length along all three axes, we must preprocess images before conducting quantitative analysis. In our anisotropic voxels, the y-axis (slice thickness of 0.6 mm/px) provides the best resolution in the volumetric data set and we adjust pixel sizes (0.72 x 0.72 mm) in the xz-plane to obtain isotropic voxel sizes of 0.6 mm per voxel. We apply a nearest neighbor resampling algorithm in the freely available open-source software ImageJ to increase the pixel number in the xz-plane without creating artificial intensity values. This crucial preprocessing step was first described in *Poppe et al.* (2019), but was not applied in *Zwaan et al.* (2018).

For the multi-pass DVC analysis, we use sub-volume sizes of 128 pixels per sub-volume side with an overlap of 50% (i.e., 64 pixels per sub-volume side) for the first step (FFT; spectral domain). Further iterations (DC; spatial domain) subsequently decrease sub-volume sizes to 64, 32 and 16 voxels with overlaps of 50% and 75%, respectively for the final step (Figure 2d). Since sub-pixel displacements are not captured by a discrete correlation peak, fitting of a Gaussian surface allows for sub-voxel displacement estimates. With the final sub-volume of 16 voxels, each displacement vector represents a discrete volume of 9.6 x 9.6 x 9.6 mm or 0.9 cm^3 (given a voxel size of 0.6 x 0.6 x 0.6 mm). Using a final overlap of 75%, we obtain displacement vectors every second voxel resulting in a spatial vector resolution of 2.4 mm. Finally, the sub-volume displacement vectors that are obtained are assembled to construct incremental (here dt = 20 min) 3D displacement fields. A detailed overview of the used DVC parameters can be found in *Schmid et al.* (2024).

We detect spurious displacement vectors in incremental displacement fields by applying an outlier detection algorithm with a local 5 x 5 neighborhood and noise threshold level of 0.1 px (*Westerweel and Scarano*, 2005). The applied algorithm removes outliers if the combined fluctuation from each displacement component is larger than the detection criterion of 0.8 and replaces outliers using an inpainting algorithm (*D'Errico*, 2008). The relatively high vector resolution resulting from final sub-volumes of 16 voxels comes at the costs of higher random noise (*Wieneke*, 2015). To reduce noisy patterns in the incremental DVC data, we apply convolution using a 3 x 3 x 3 smoothing kernel that replaces the center vectors with the local average of the vectors in the kernel. With the kernel size being smaller in spatial dimensions (7.2 x 7.2 x 7.2 mm) than the final sub-volume (9.6 x 9.6 x 9.6 mm), additional lowpass filtering is minimized (*Raffel et al.*, 2018).

Finally, we sum up incremental displacement components of subsequent time increments to obtain finite displacement components u_x, u_y, and u_z. Before the summation of the incremental displacement components, we employ a natural-neighbor interpolation scheme (*Amidror*, 2002) to accommodate material advection (Lagrangian summation). In addition, we provide 1 h increments (i.e., individual displacement components of 20 min increments summed up hour-wise) in Supporting Information SI-1-SI-3.

2.4 DVC Error Estimation and Comparison with *Zwaan et al.* (2018) Data

For quantifying mean and standard deviation (SD) of the error of each displacement component, we employ a test sample to investigate the performance of the improved DVC approach. We test four configurations with different DVC parameters including the parameters of both the new (this study) and old approach (*Zwaan et al.*, 2018). The rectangular PVC test box is filled with identical viscous and brittle materials as used in the original experiment and we XRCT-scan the sample 5 times using the identical XRCT parameters applied in *Zwaan*

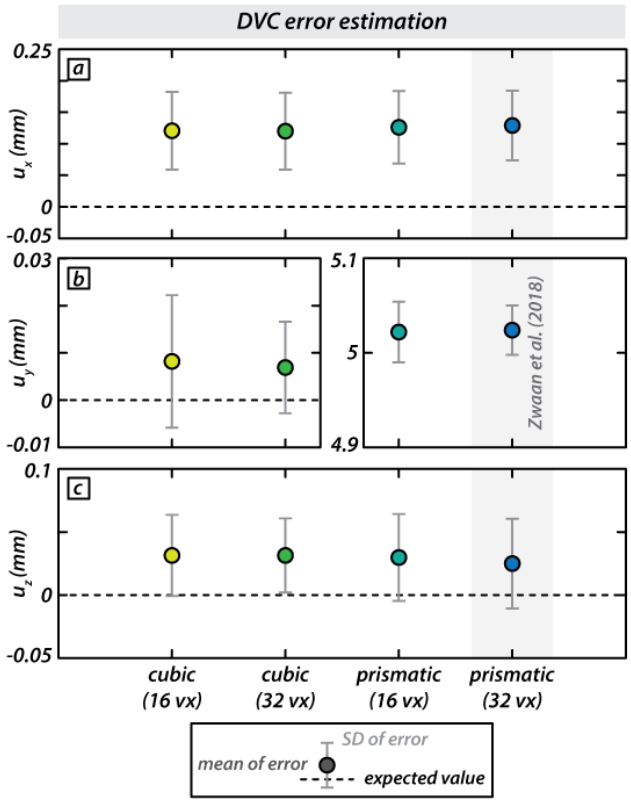

Figure 3 – DVC error estimation obtained from test sample. Four sets are tested for cubic sub-volumes consisting of 16 (this study) and 32 voxel sizes, and prismatic sub-volumes consisting of 16 and 32 (*Zwaan et al.*, 2018) voxel sizes. **a)** Mean of error and std of error for displacement component u_x. **b)** Mean of error and std of error for displacement component u_y. **c)** Mean of error and std of error for displacement component u_z.

et al. (2018). After the first scan procedure, the box is moved parallel to the y-axis (see Figure 2) by 5 mm (by programming the XRCT-bed) and rescanned 5 times. The respective 5 scans are stacked and preprocessed accordingly to reproduce DVC-ready data sets from *Zwaan et al.* (2018) and this study. The final XRCT-data set from *Zwaan et al.* (2018) contains prismatic voxels with dimensions of 0.72 x 0.3 x 0.72 mm/px on which DVC is performed using final sub-volumes of 32 voxels (prismatic 32 vx; Figure 3). The final XRCT-data set of our study yields cubic voxels with dimensions of 0.6 x 0.6 x 0.6 mm/px on which DVC is performed using final sub-volumes of 16 voxels (cubic 16 vx; Figure 3). For the sake of completeness, we also test XRCT-data sets containing cubic and prismatic voxels, on which we perform DVC using sub-volumes of 32 voxels (cubic 32 vx; Figure 3) and 16 voxels (prismatic 16 vx; Figure 3), respectively.

Since the test sample is only moved along the y-axis by 5 mm between the two XRCT scans, DVC results for each XRCT data set, should yield expected displacements of 0 mm within the xz-plane and 5 mm along the y-axis with a standard deviation of 0 for each displacement component. Note that, the sample box is not moved along the x- and z- axis since sufficient accuracy cannot be assured when moving the sample box manually. We calculate the mean of error for each displacement component as

$$Error\ \bar{u}_{x,y,z} = \left|\bar{u}^{DVC}_{x,y,z} - \bar{u}^{expected}_{x,y,z}\right|, \quad (1)$$

where $\bar{u}^{DVC}_{x,y,z}$ is the mean of the respective displacement component obtained from DVC and $\bar{u}^{expected}_{x,y,z}$ denotes the expected mean displacement values for the respective displacement component.

Table 1 – Mean and standard deviation of the error for displacement components u_x, u_y, and u_z.

measure (mm)	cubic (16 vx)	cubic (32 vx)	prismatic (16 vx)	prismatic (32 vx)
Error $\bar{u}_x$	0.121	0.120	0.126	0.129
1 SD $\bar{u}_x$	0.063	0.063	0.059	0.057
Error $\bar{u}_y$	0.008	0.007	5.022	5.024
1 SD $\bar{u}_y$	0.014	0.010	0.033	0.027
Error $\bar{u}_z$	0.031	0.031	0.030	0.025
1 SD $\bar{u}_z$	0.033	0.030	0.035	0.036

The mean of error and the 1 SD of error for all four tested configurations are listed in Table 1 and shown in Figure 3. For all four configurations, mean and standard deviation of the error are consistent. This shows that the choice of the final sub-volume size does not affect the results since displacement solutions from adjacent vectors strongly correlate due to the overlap of the sub-volumes. However, there is a critical difference between the mean of error of u_y for cubic and prismatic voxels (Figure 3b). While the mean of error for cubic voxels is close to 0 (expected value of 5 mm and SD $\pm$0.03 mm), prismatic voxels systematically overestimate the expected value by a factor of 2. This overestimation is a direct result of the anisotropic voxel size of 0.72 x 0.3 x 0.72 mm/px and was accounted for in *Zwaan et al.* (2018) post-DVC analysis. Note that, the values presented in Table 1 result from non-deformed samples providing an idealized case and likely underestimate values from experiments where material deforms (*Thielicke*, 2014).

2.5 Analysis of Internal Deformation and Visualization

To analyze the model's internal deformation, we first make use of cumulative displacement components u_x (horizontal), u_y (horizontal), and u_z (vertical) to describe the general evolution. Cumulative displacement components represent the finite shape at the final experiment stage (i.e., after 4 h). Additionally, we provide incremental displacement components (i.e., increments of 1 h) in Supporting Information SI-1-SI-3. The entire DVC analysis provides an extensive data set, which is available in an additional data publication (*Schmid et al.*, 2024). We present data from three distinct model transects (A-A', B-B' and C-C'; see Figure 2c). Compared to *Zwaan et al.* (2018) we additionally use horizontal model slices from the brittle layer (F-F'), near the

brittle-viscous interface (G-G'), and from the viscous layer (H-H') to investigate the deformation at different depth levels (Figure 2c). Note that, strictly speaking, the brittle-viscous interface does not occur as a flat horizontal plane but builds an irregular surface due to the viscous seeds that deform over time. However, since the horizontal data slice G-G' captures most of the brittle-viscous boundary, we use it as a practical means to study the brittle-viscous interface.

Note that, in the original study by *Zwaan et al.* (2018), the model was not perfectly horizontally positioned during XRCT scans and favored gravitationally-driven out-of-plane flow near the left rift segment. As a result, the horizontal displacement component u_y showed a stronger flow towards the observer at any time compared to u_y away from the observer. We correct the u_y component by subtracting the mean u_y flow over the entire model domain assuming that this does not substantially change the outcome of rift-axis parallel flow.

2.5.1 Calculation of Finite Stretch and Rotation

For further investigating deformation and rigid body rotation, we export the DaVis inherent displacement data as .txt files of subsequent time steps and process 3D displacement data in MATLAB.

First, we assemble the deformation gradient tensor F using the relationship:

$$F = I + H = \begin{bmatrix} 1+\frac{\partial u_x}{\partial X_x} & \frac{\partial u_x}{\partial X_y} & \frac{\partial u_x}{\partial X_z} \\ \frac{\partial u_y}{\partial X_x} & 1+\frac{\partial u_y}{\partial X_y} & \frac{\partial u_y}{\partial X_z} \\ \frac{\partial u_z}{\partial X_x} & \frac{\partial u_z}{\partial X_y} & 1+\frac{\partial u_z}{\partial X_z} \end{bmatrix}, \quad (2)$$

where I and H are the identity matrix and displacement gradient tensor, respectively. The deformation gradient tensor components $\frac{\partial u_i}{\partial X_j}$ refer to the components u_i (i.e., u_x, u_y, u_z) of the displacement field with respect to the initial coordinate components X_j (i.e., X_x, X_y, X_z) in 3D (e.g., *Allmendinger et al.*, 2011).

The relatively large time increments (i.e., 20 min) possibly lead to substantial deformation between subsequent XRCT scans (given a 2.5 mm extension for each increment). Therefore, the use of infinitesimal strains is problematic since the linear strain approximation no longer holds if large rotations and simple strains occur. These limitations of the infinitesimal strain tensor have been lucidly demonstrated in *Broerse et al.* (2021). Alternatively, finite strain tensors are insensitive to rotations and consider shear-induced extension. The use of finite stretches and rotations, therefore, provides a better choice considering the large time increments and the amount of rotation in the presented model (Figure 4). The left polar decomposition decomposes the deformation gradient tensor F into a product of a symmetric 3 x 3 stretch tensor and an orthogonal rotation tensor

$$F = V \times R, \quad (3)$$

where V denotes the left stretch tensor providing the shape change in the final state after applying the rotation R (e.g., *Malvern*, 1969). The principal stretch values λ_i of V represent the axes of the 3D strain ellipsoid and are directed in the stretch directions in the final deformed state (*Broerse et al.*, 2021). Since V is related to the left Cauchy-Green deformation tensor $B = F \times F^T$, its principal stretch values λ_i can be obtained from the principal values μ_i of B by

$$\lambda_i = \sqrt{\mu_i}. \quad (4)$$

From the principal stretches, we obtain the maximum possible shear γ_{max} as

$$\gamma = \lambda_1 - \lambda_3, \quad (5)$$

with λ_1 and λ_3 being the largest and smallest stretch magnitudes (e.g., *Broerse et al.*, 2021). The maximum possible shear is suitable to quantify shear in the presented model as it is not affected by rigid body rotation. Furthermore, the maximum possible shear is base invariant and its magnitude is not dependent on the choice of reference coordinate system.

Tensor R applies a rotation to the initial coordinates before applying the left stretch tensor V. Note that, R does not only contain rigid body rotation but also rotational components due to (simple) shear (*Broerse et al.*, 2021). The amount of shear contribution within the rotation tensor R depends on the magnitude of the off-diagonal components of the stretch tensor V. In our experiment, off-diagonal terms are generally negligible and only increase near the rift branches and the brittle-viscous interface. Hereafter, we therefore refer to rotation as quasi-rigid body rotation.

The Euler angle vector is defined by

$$u = [\phi, \theta, \psi] \quad (6)$$

and contains angles ϕ, θ, and ψ of sequential intrinsic rotations about axes *i*, *j*, and *k*, respectively (e.g., *Diebel*, 2006). The function that maps an Euler angle vector to its corresponding rotation matrix R_{ijk} depends on the sequence of coordinate rotations. Note that, axes *i*,*j*, and *k* rotate and hence, change their orientation with respect to the initial reference coordinate system. Since we are interested in rotations about the vertical coordinate axes z, we use the Euler Angle sequence (1,2,3; i.e., Cardan angles) such that the first rotation $R_k(\psi)$ coincides with a rotation about the initial coordinate axes z (*Diebel*, 2006, eq. 72):

$$u_{123}(R) = \begin{bmatrix} \phi_{123}(R) \\ \theta_{123}(R) \\ \psi_{123}(R) \end{bmatrix} = \begin{bmatrix} \arctan 2(r_{23}, r_{33}) \\ -\arcsin(r_{23}) \\ \arctan 2(r_{12}, r_{11}) \end{bmatrix} \quad (7)$$

where the Euler angle $\psi_{123}(R)$ describes the rotation about the initial vertical model axis (i.e., z-axis).

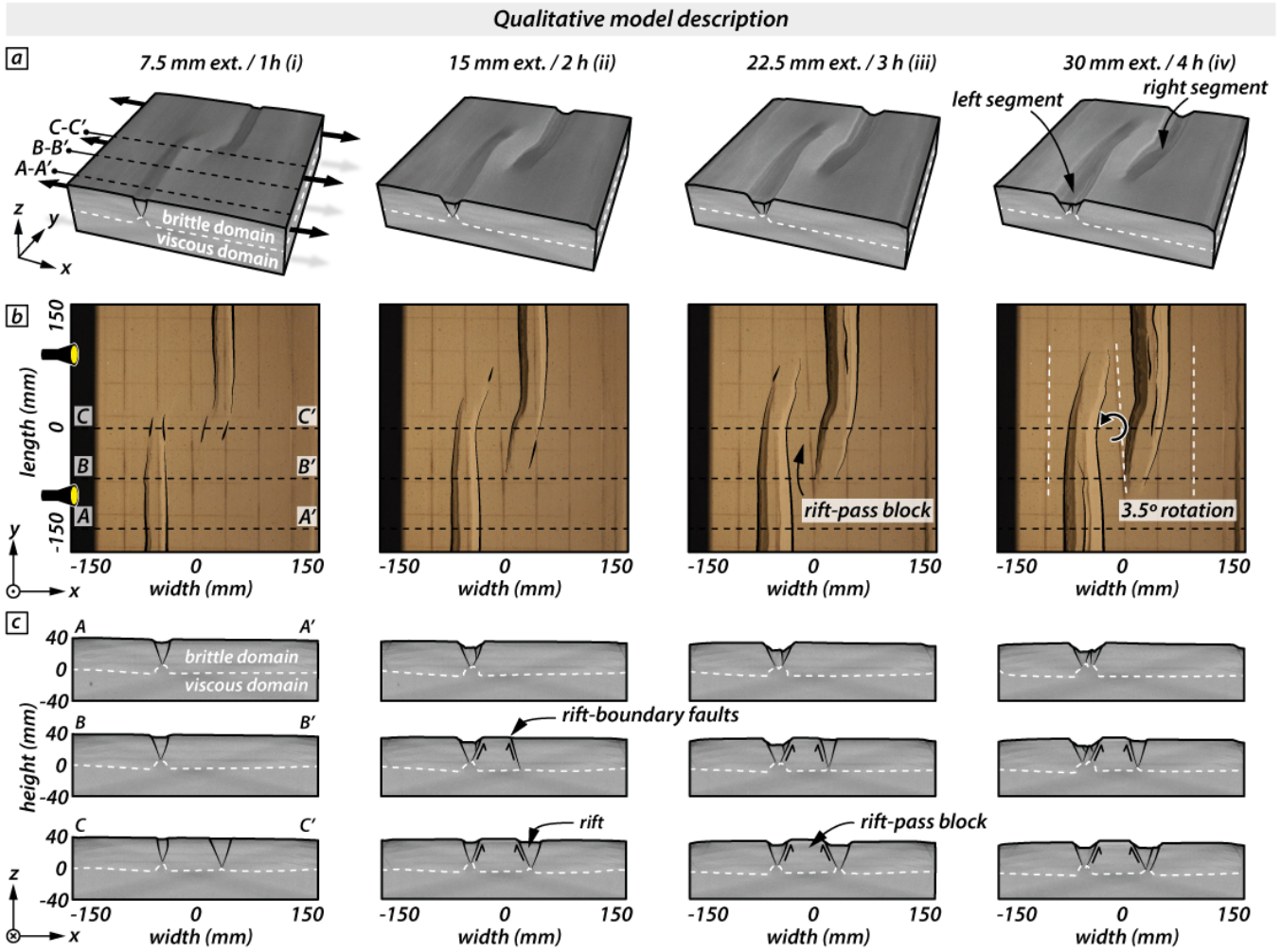

Figure 4 – Qualitative model description using XRCT volumes, top view imagery, and XRCT slices at profile lines indicated in top views at distinct model stages (i.e., every hour). **a)** XRCT volumes of the analyzed rift-pass model. Dashed black lines indicate the positions of model transects A-A', B-B', and C-C', and black arrows indicate extension direction. Dashed white lines indicate the brittle-viscous interface. **b)** Top views of the rift-pass model. Black dashed lines indicate the positions of model transects used to present DVC results. The light source is positioned on the left side of the model and casts shadows for visualizing deformation structures. A fine 4 by 4 cm grid of corundum sand was sieved on the surface before the model run for visual aid. The rotation of the grid reveals a counter-clockwise block rotation of about 3.5° at the final model stage. **c)** XRCT slices at model transect positions A-A', B-B', and C-C' at distinct model stages. White dashed lines indicate the brittle-viscous interface that divides the model into an upper brittle and a lower viscous layer. Faults are indicated by black lines for better visibility. Black arrows indicate the relative uplift of the rift-pass block.

Finally, we locate the vertical rotation axis where the total horizontal displacement in the brittle layer is near zero (i.e., $\sqrt{U_x^2 + U_y^2} \approx 0$) and define an area with radius $r \leq 2$ cm around the rotation axis. Subsequently, rotation values R_z of all data points within this area are averaged slice-wise and represent the mean rotation about the vertical model axis for each time step.

2.5.2 Kinematic Coupling Between Brittle and Viscous Model Layers

Multiple definitions of dynamic coupling between brittle and viscous layers are used in the literature: For example, *Brun* (1999) describes coupling between brittle and viscous model layers as a function of the applied strain rate. At lower strain rates, deformation within the viscous layer can occur at low stresses allowing the viscous layer to act as a décollement whereas higher strain rates increase the viscous layer strength and force similar deformation styles in the brittle and viscous model domains. *Schueller et al.* (2010) use the term brittle-ductile coupling to describe the interaction between ductile viscosity and brittle softening and the resulting different fracturing modes in the overburden. However, dynamic coupling is difficult to assess in analogue experiments since required information about stresses can only be assumed. For example, *Zwaan et al.* (2019) describe the dynamic coupling between brittle and viscous model layers and the basal setup using the initial differential stress in respective model setups. All the above-stated approaches have in common that they describe coupling partly as a function of the viscous strength (i.e., differential stresses in the viscous domain) that may change over time and lead

to different degrees of coupling over time.

Here, we use the term *kinematic coupling* to describe the differences in motions in the brittle and viscous model layers. Displacement components obtained from our DVC analysis allow for the investigation of spatial variations of kinematic coupling between the brittle and viscous model layers as expressed by spatially varying maximum possible shear γ_{max} (see Section 2.5.1). Particularly, we investigate γ_{max} (i.e., $\lambda_1 - \lambda_3$) at the brittle-viscous interface and normalize γ_{max} over the entire model domain such that values range between 0 (i.e., areas with no shear) and 1 (i.e., areas with high shear). Normalized γ_{max} allows to investigate which parts of the brittle-viscous interface show enhanced (i.e., $\gamma_{max} = 0$) and low (i.e., $\gamma_{max} = 1$) degrees of kinematic coupling between the brittle and viscous model layers.

3 Results

3.1 Qualitative Evolution from Top Views and XRCT Imagery

The evolution of the model is qualitatively illustrated by top view photographs and XRCT imagery in Figure 4. In the following, we briefly describe characteristic stages of rift evolution: XRCT volumes (Figure 4a) and top views (Figure 4b) show the model's evolution at successive 7.5 mm extension increments (i.e., every hour of the model run, indicated by roman letters). After 7.5 mm extension (i.e., 1 hour; Figure 4 (i)) normal faulting initially localizes above each seed forming two rift segments. Near the model center (i.e., at y = 0 mm) the tips of each rift segment propagate in a curved fashion towards each other. With increasing extension, the rift segments propagate laterally and pass one another (i.e., 15 mm extension after 2 hours; Figure 4 (ii)). The curved character of the propagating rift segments creates a rift-pass block (*Nelson et al.*, 1992) in between them. This rift-pass block undergoes a slight counter-clockwise rotation of ∼3.5° about a vertical axis during progressive extension (Figure 4b (iv)).

XRCT model transects at successive time steps show model internal evolution at three distinct positions within the model (i.e., A-A', B-B' and C-C'; Figures 2c, 4c). Note that, due to the experiment setup, deformation evolution is reasonably symmetric (i.e., point symmetry with respect to the model center coordinates x = 0, y = 0). The expected deformation features on either side of the y-axis are fairly identical and therefore, the three transects only capture half the model domain (i.e., the part where y = -150 – 0 mm). As normal faults form above the seeds, rift basins develop after some 40 to 60 min, or 5 to 7.5 mm of extension (Figure 4c (i)). XRCT sections also show how rift segments propagate laterally, start to overlap and form a rift-pass block undergoing relative uplift in between the overlapping rifts (Figure 4c (i-iii) black arrows). Each rift segment is bounded by two major normal faults that show decreasing throw towards the rift tips. Rift structures are more complex above the initial seeds with more internal faulting than near the rift tips. The dip of the main rift boundary faults decreases with time, from initially ∼70 to ∼60° towards the end of the experiment (Figure 4c (iv)). Over the course of the model run, the viscous material flows, and the seed becomes larger while also rising to the surface along the basin axis.

3.2 DVC Results

The following subsections focus on the quantitative description of shape changes (using finite displacement components u_x, u_y, and u_z) and rotation (i.e., about a vertical axis). Moreover, we quantify kinematic coupling between brittle and viscous model layers using the maximum possible shear (γ_{max}), that depicts distinct shear planes (i.e., fault zones and décollements between the brittle and viscous model layers).

3.2.1 Overview of Final Cumulative Displacement Components and Maximum Possible Shear in Model Transects

Cumulative displacement components u_x, u_y, and u_z best describe the shape at the final model stage (i.e., after 4h of model run). Maximum possible shear γ_{max} visualizes faulting and shearing in the brittle and viscous model layers, respectively.

The horizontal displacement component u_x displays motion perpendicular to rift segment axes (i.e., horizontal motions parallel to the direction of applied divergence velocity field; Figure 5a-c). Maximum u_x values at the final model stage are ∼15 mm. From transect A-A' (Figure 5a) to transect C-C' (Figure 5c) a distinct change occurs in u_x displacement patterns. At transect A-A', the rift structure in the brittle layer separates left-moving and right-moving domains to the left and right of the left rift segment, respectively (Figure 5a). Maximum u_x values of ∼15 mm occur in the viscous layer close to the sidewalls. In the central part of the viscous layer (i.e., from -60 mm to 30 mm) a pocket with reversed u_x values occurs; viscous material to the left of the viscous seed flows towards the right (i.e., towards the rift axis) and vice versa (Figure 5a). For the intermediate model transect B-B' (Figure 5b) this flow reversal is still visible in the viscous layer below the left rift segment. In the brittle layer, low u_x values of ∼3 mm indicate the rift-pass block, bounded by the two rift segments (Figure 5b). Model transect C-C' (Figure 5c) shows a symmetrical pattern where maximum u_x values occur close to the sidewalls in the viscous layer. Below the two rift segments, u_x values are close to 0. The brittle layer shows homogeneous u_x values with high gradients along the rift boundary faults and the stable rift-pass block in the model center (Figure 5c).

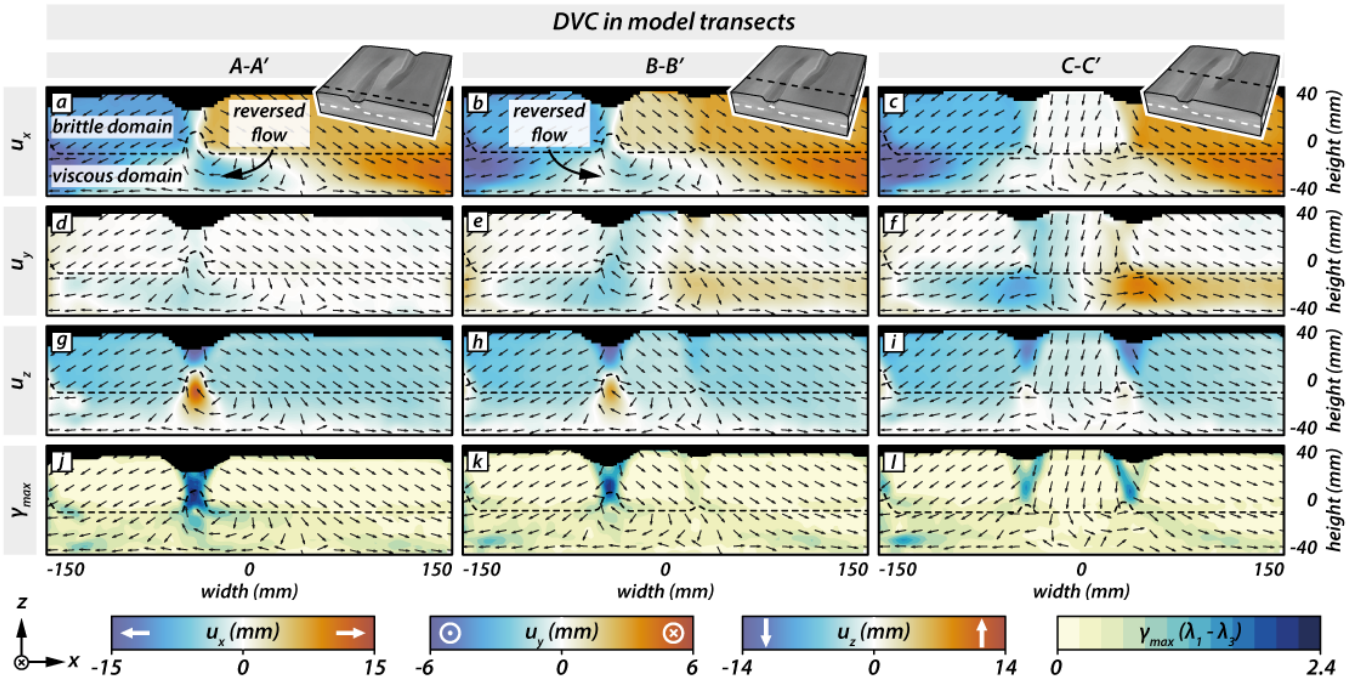

Figure 5 – DVC maps of finite displacement components u_x, u_y, u_z, and maximum possible shear γ_{max} at the final model stage after 30 mm bulk extension (i.e., after 4h) for model transects A-A', B-B', and C-C'. The DVC maps depict a change from an asymmetrical displacement distribution at transect A-A' to a symmetrical distribution at transect C-C'. **a-c)** Horizontal u_x displacement maps for all three model transects. **d-f)** Horizontal u_y displacement component maps. **g-i)** Vertical u_z displacement maps. **j-l)** Maximum possible shear γ_{max}. Dashed black lines indicate the brittle-viscous interface. Vectors indicate the 3D finite displacement field projected onto the xz-plane (vectors have all unit lengths for better visibility). White lines indicate zero-displacement. Direction markers in color bars indicate relative motion with respect to the xz-plane.

The horizontal displacement component u_y (Figure 5d-f) displays motion perpendicular to the xz-plane and the direction of applied divergence velocity field (i.e., towards and away from the reader indicated by positive and negative values, respectively). The u_y component (max values ~6 mm), a factor of ~3 smaller than the u_x component, is highest in the viscous layer below the rift segments in all transects. While u_y values in the brittle layer are close to 0, material below the left rift segment in the viscous layer moves out of the section, towards the observer with values of ~-6 mm. Below the right rift segment, counter flow (i.e., away from the observer) occurs in the central model transect C-C' (Figure 5f) with u_y values of ~6 mm and lower values in transect B-B' (Figure 5e). In transect A-A', such counter flow does not occur and the right rift segment is not developed (Figure 5d).

The vertical displacement component u_z (Figure 5g-i) is most prominent in the viscous layer below the seeds. Zones of maximum u_z values of ~14 mm indicate strong upward flow of the viscous material while the brittle material above thins. While in model transect A-A' (Figure 5g) upward flow with u_z values of ~14 mm is strongest, model transect B-B' (Figure 5h) shows less pronounced upward flow with maximum u_z values of ~10 mm. In the central transect C-C' (Figure 5i), upward flow is minor but occurs evenly localized below both rift segments. Largest subsidence values occur in the rift segments where granular material is vertically displaced due to brittle faulting (Figure 5g-i). Note that, all three model transects are dominated by a background subsidence throughout the model due to the overall thinning of the viscous layer during extension.

Maximum possible shear γ_{max} highlights brittle faulting along rift-boundary faults in all three transects with maximum values of 2.4 (Figure 5j-l). While γ_{max} in the brittle layer is mainly localized along faults, the viscous layer contains diffuse patterns. Almost in the entire viscous layer shear values of 0.5 occur, indicating that horizontal viscous flow values (i.e., u_x and u_y) exceed horizontal motions in the brittle model layer. In the central model transect C-C' (Figure 5l) shear values below the rift-pass block, however, are reduced with values of ~0.2 indicating minor to no relative horizontal motion of the rift-pass with respect to the viscous layer.

3.2.2 Overview of Final Cumulative Displacement Components and Maximum Possible Shear in Horizontal Slices

Horizontal slices (Figure 6) in the brittle layer (Figure 6a, d, g, j), near the brittle-viscous interface (Figure 6b, e, h, k), and in the viscous layer (Figure 6c, f, i, l) provide additional insights into displacement components and γ_{max}. In the brittle layer the rift boundary faults determine the positions of jumps in the displacement component u_x (Figure 6a). In the central part of the brittle layer, the rotating rift-pass

block is well visible due to the counter clockwise rotational vector pattern. Near the brittle-viscous interface (Figure 6b) u_x gradients are more diffuse and a clear rotation center is absent. u_x values in the viscous layer (Figure 6c) depict the flow reversal in the displacement direction that is also visible in model transects (Figure 5a-c).

The prominent out-of-plane (u_y) motion seen in model transects (Figure 5d-f) becomes more expressed in horizontal slices (Figure 6d-f). At the final model stage (i.e., after 4h of model run) maximum u_y values in the rift segments are ~3 mm and show opposite displacement directions for each segment in the brittle layer (Figure 6d). At the brittle-viscous interface, u_y values increase (up to ~5 mm) compared to the brittle layer and are less localized (Figure 6e). Maximum u_y values of ~6 mm occur throughout the viscous layer (Figure 6f). Here, two distinct and opposing flow directions develop on the left (i.e., x $\leq$ 0 mm) and right (i.e., x $\geq$ 0 mm) model side, respectively, accompanying the counter clockwise rotation of the rift-pass block in the brittle layer above (Figure 6a, f).

Horizontal slices of the vertical displacement component u_z clearly visualize localized differential vertical motions in the brittle and viscous layers with maximum values of ~14 mm (Figure 6g-i). In the brittle layer (Figure 6g), subsidence is strongly localized within the rift segments. At the brittle-viscous interface (Figure 6h), strong upward flow occurs along the viscous seeds, where viscous material rises to compensate for extension and subsequent faulting in the brittle model layer. In the viscous layer (Figure 6i) a similar pattern can be observed. However, zones of vertical displacement are more diffuse indicating more distributed upward flow of the viscous material in contrast to the seed tips at the brittle-viscous interface (Figure 6h). This is also illustrated by the vertical u_z displacement in model transects (Figure 5g-i). In contrast to localized upward flow in the viscous layer, the overall vertical displacement shows homogeneous subsidence due to the thinning of the viscous layer with progressive extension.

In the brittle model layer, maximum γ_{max} values of 2.4 depict the two rift segments that confine the rift-pass block (Figure 6j). Apart from the rift segments, γ_{max} values near zero indicate that shearing in the brittle layer is strongly localized and no shear occurs outside the rift segments apart from minor shear at the left model margin due to boundary effects. At the brittle-viscous interface, γ_{max} values are generally more diffuse and are highest (~1.2) below the rift segments near the viscous seeds (Figure 6k). In the viscous model layer, γ_{max} values are low (~0.8) with maximum values near the viscous seeds (Figure 6l).

3.3 Rotation About the Vertical Axis in the Brittle Layer

Top views of the model evolution show a counter-clockwise rotation of the rift-pass block of ~3.5° about a vertical axis (Figure 4b). The horizontal displacement vector field (i.e., u_x, u_y) supports this observation (Figure 6a) and shows the rotation axis of the rift-pass block near the coordinate origin. From the displacement vector field solely, one cannot discriminate if such a rotation is due to a purely rigid-body rotation or caused by additional simple shear. Even so, the assumption that the rift-pass block rotates en masse seems reasonable (see Section 2.5.1). Moreover, Figure 7a indicates that γ_{max} values in the brittle layer only occur at the rift segments that confine the rift-pass block without any evidence for shear inside the rift-pass block itself. Figure 7b shows the rotation R_z about the vertical z-axis and constrains a central area (i.e., the rift-pass block) that undergoes counter-clockwise rotation within a range of 0° to 6°. Note that, adjacent to the rift-pass block (i.e., at the rift segments), R_z depicts clockwise rotation indicating right-lateral simple shear at the u_y displacement peaks (Figure 6d).

Using all horizontal DVC data slices through the brittle model layer (Figure 7c), mean R_z values (taken in the vicinity of the rotation axis; see Section 2.5.1) gradually increases up to a mean value of ~3.3°, which is reasonably consistent with the rotation of ~3.5° observed at the surface (Figure 4b (iv)). This corresponds to an average rotation rate of ~0.8° h^{-1}. Note that, within the first 1.5 h of the model run, rotation rates are slightly higher compared to the remaining run time. Further, quasi-rigid body rotation values from all horizontal slices range between ~2.5 and 3.5° indicating that the rift-pass block rotates en masse and energy dissipation (i.e., shearing within the rift-pass block) is negligible (Figure 7a).

3.4 Rotation About the Vertical Axis in the Viscous Layer

Values of R_z observed in the brittle layer gradually decrease downward into the viscous layer (Figure 8). In contrast to the brittle layer, γ_{max} values in the viscous layer show a more diffuse pattern with maximum values of ~0.8 below the viscous seeds and values near zero in the central model part below the rift-pass block (Figure 8a). Hence, shear clearly contributes to R_z that can no longer be described as quasi-rigid body rotation; although the horizontal slice H-H' in the viscous layer still shows partly rotation below the rift-pass block with maximum R_z values of about 2° (Figure 8b), the area is less confined compared to the brittle layer. R_z values of all horizontal slices in the viscous layer (taken in the vicinity of the rotation axis; see Section 2.5.1) show a gradual increase in flow with a mean value of ~1.1° after 4h of model run (Figure 8c). In contrast to the brittle layer, mean R_z values are more

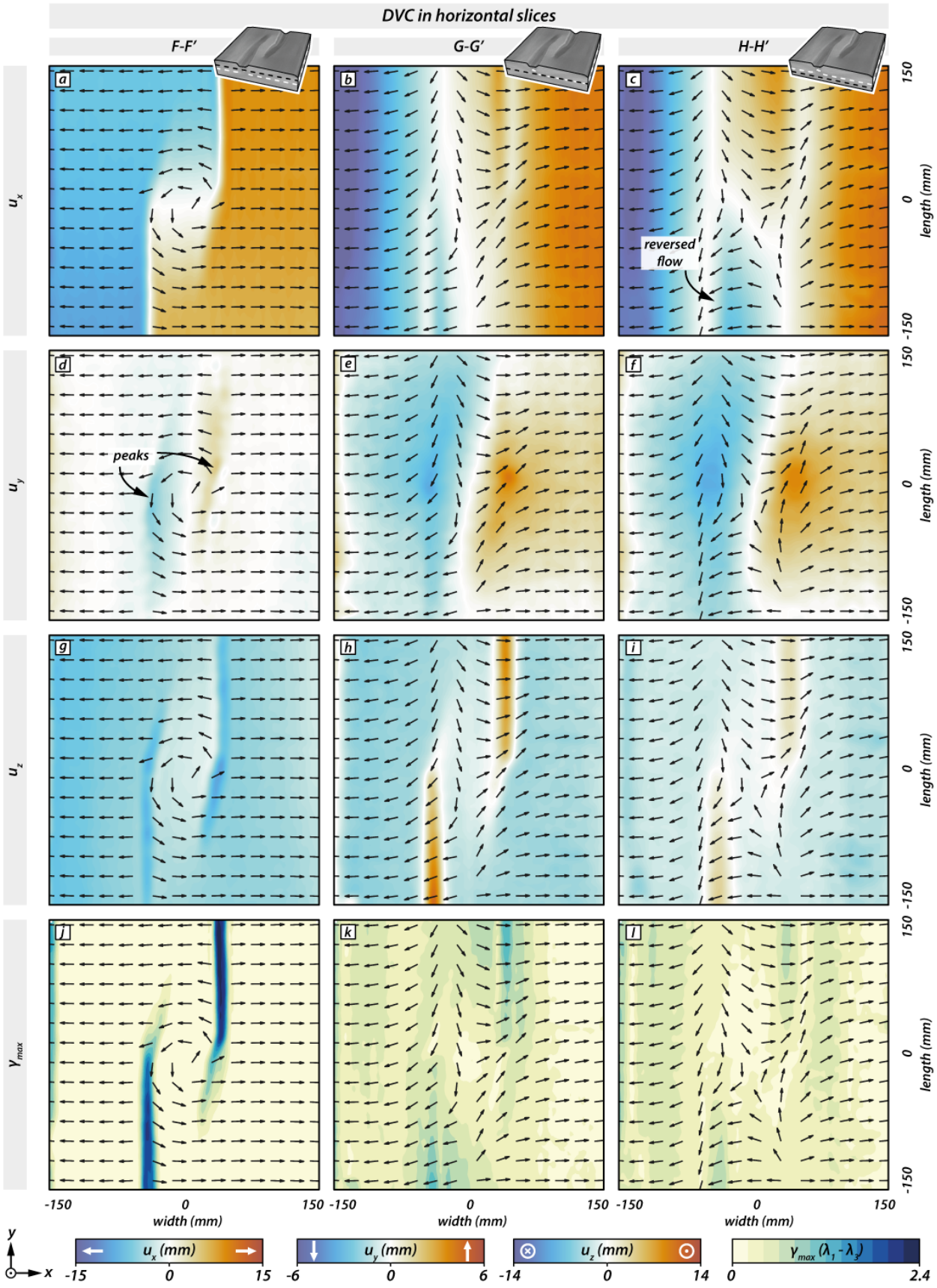

Figure 6 – DVC maps of finite displacement components u_x, u_y, u_z and maximum possible shear γ_{max} at the final model stage after 30 mm bulk extension (i.e., after 4h) for horizontal slices F-F′ (brittle layer), G-G′ (brittle-viscous interface), and H-H′ (viscous layer). **a-c)** Horizontal u_x displacement maps for all three horizontal slices. **d-f)** Horizontal u_y displacement component maps. **g-i)** Vertical u_z displacement maps. **j-l)** Maximum possible shear γ_{max}. Vectors indicate the 3D finite displacement field projected onto the xy-plane (vectors have all unit lengths for better visibility). White lines indicate zero-displacement areas. Direction markers in color bars indicate relative motion with respect to the xy-plane. White contour lines indicate zero-displacement.

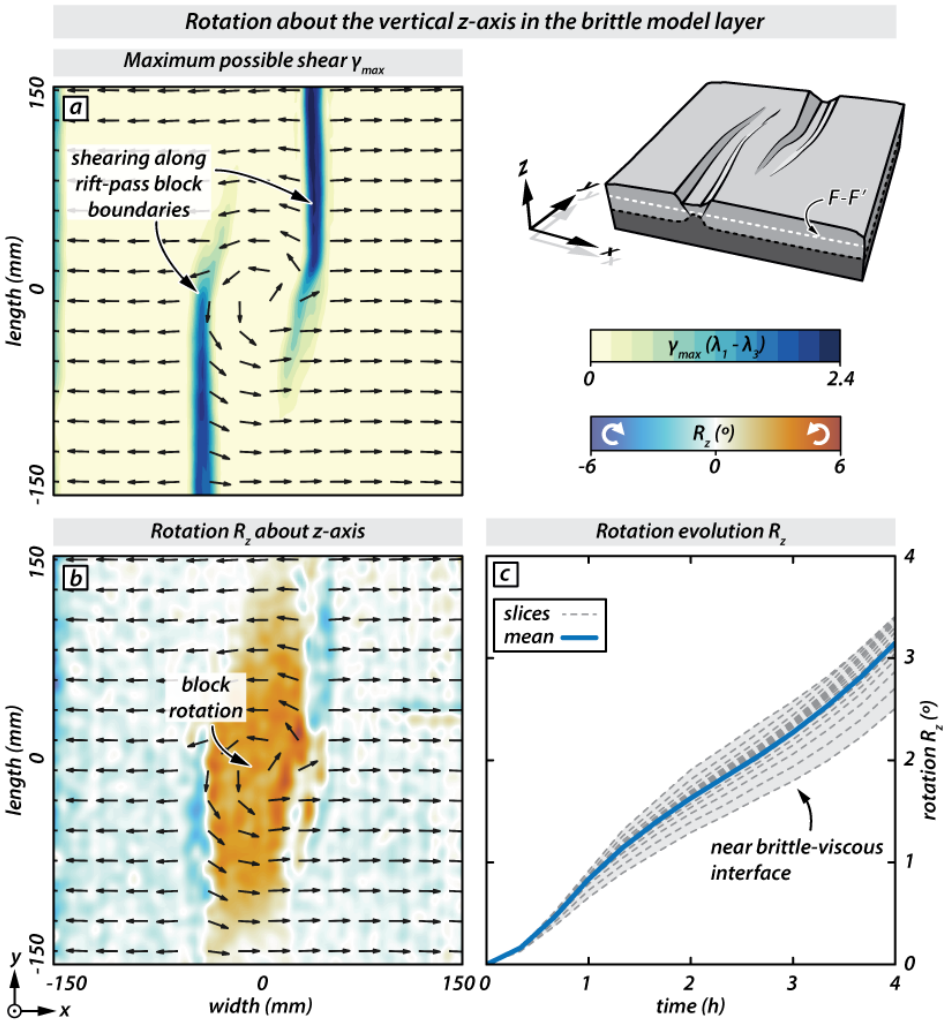

Figure 7 – Rotation component R_z of the rift-pass block about a vertical axis at the final model stage (i.e., after 4h) in the horizontal slice F-F'. **a)** Maximum possible shear γ_{max} in the horizontal slice F-F'. High shear values occur along the rift branches confining the rift-pass block. **b)** Rotation about the vertical axis of the rift-pass block indicated by the rotation component R_z. **c)** Evolution of block rotation for all horizontal slices in the brittle layer (dashed, grey lines) and mean block rotation averaged over the entire brittle model domain (blue line). Vectors in a) and b) indicate the 3D finite displacement field projected onto the xy-plane (vectors have all unit length for better visibility). White contour lines in b) indicate zero rotation. Direction markers in color bar indicate the sense of rotation with respect to the xy-plane.

dispersed in the viscous layer ranging from 0.25 to 2° and gradually increase towards the brittle-viscous interface.

3.5 Kinematic Brittle-viscous Coupling near the Brittle-ductile Interface

Above, we document quasi-rigid body rotation in the brittle layer gradually decreasing in the underlying viscous layer with a substantial simple shear contribution. The increasing contribution of shear within the viscous model layer implies that the brittle-viscous interface acts as a horizon, where the two layers (partially) decouple (see our definition of kinematic brittle-viscous coupling in Section 2.5.2.).

The brittle-viscous interface shows a fairly point-symmetric (i.e., with respect to the model center) variation in kinematic coupling (Figure 9). The lowest degrees of coupling (i.e., high γ_{max}) occur near the location of the viscous seeds (Figure 9a). This is related to u_z values that are of opposing directions in the brittle (i.e., subsidence) and viscous (i.e., upward flow) layers (Figure 5g). Such strong vertical u_z values largely contribute to the maximum possible shear resulting in low kinematic coupling. Towards the model center (and the center of the rift-pass block), γ_{max} values decrease and, according to our definition, indicate an increase in kinematic coupling. Note that, in the vicinity of the rotation axis, horizontal displacements (and therefore shearing) remain small at the brittle-viscous interface making it difficult to pinpoint its true state of kinematic coupling. Further away from the rotation axis, horizontal displacements increase leading to increased γ_{max} values and hence, weaker kinematic brittle-viscous coupling.

The increasing kinematic coupling towards the rotation axis is also visible in model transects (Figure 9b-d). At transect A-A' (Figure 9a, b), shearing is strongest below the brittle-viscous interface due

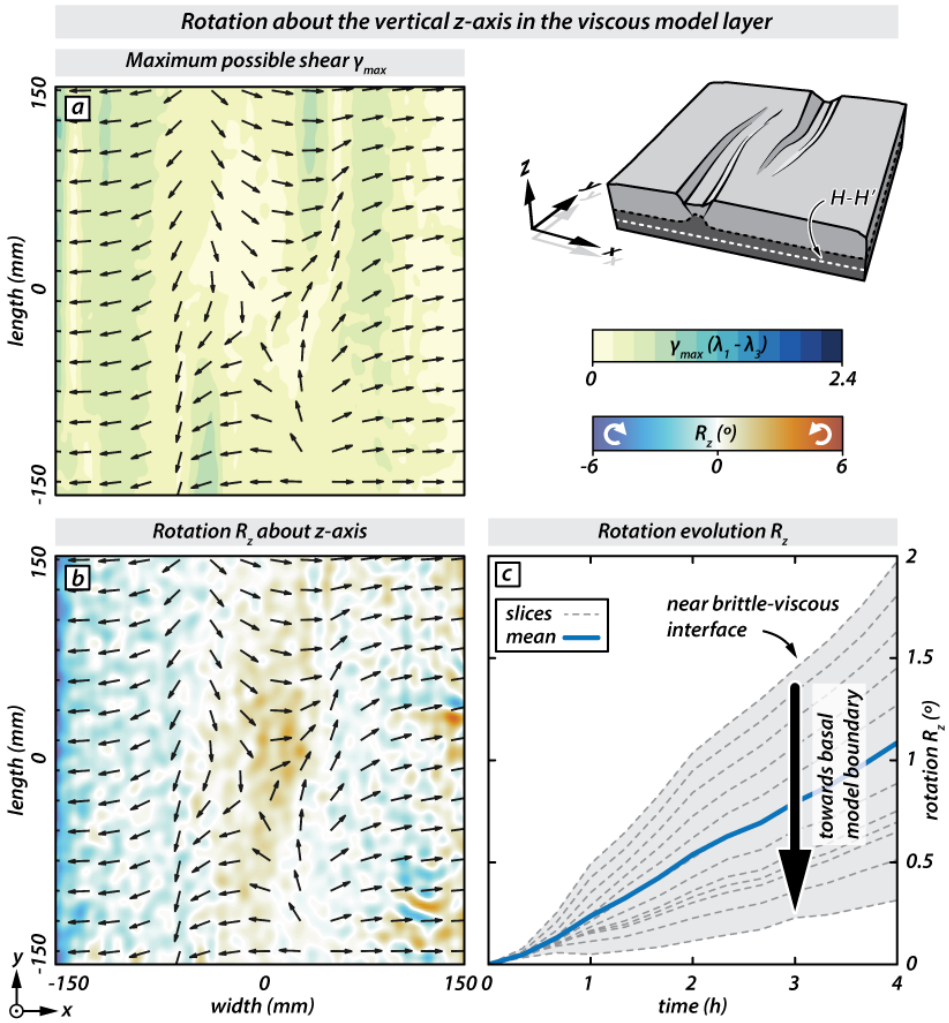

Figure 8 – Rotation component R_z of the rift-pass block about a vertical axis at the final model stage (i.e., after 4h) in the horizontal slice H-H'. **a)** Maximum possible shear γ_{max} in the horizontal slice H-H'. Shearing is dispersed in the viscous layers around the model center. **b)** Rotation about the vertical axis in the viscous layer indicated by the rotation component R_z. **c)** Evolution of rotation component R_z for all horizontal slices in the viscous layer (dashed, grey lines) and mean rotation averaged over the entire viscous model layer (blue line). Vectors in a) and b) indicate the 3D finite displacement field projected onto the xy-plane (vectors have all unit length for better visibility). White contour lines in b) indicate zero rotation. Direction markers in color bar indicate the sense of rotation with respect to the xy-plane.

to the rift-pass block rotation about the vertical axis in the brittle layer. The prominent zone of weak kinematic coupling forms a décollement below the rift-pass block that successively decreases towards the model center (Figure 9c, d). At the central transect C-C' (Figure 9d) the décollement vanishes resulting in strong kinematic brittle-viscous coupling.

4 Discussion

Analogue modelling studies that use a medical XRCT scanner clearly are of great benefit for a better understanding of tectonic processes over time and in three dimensions. The vast amount of XRCT data produced allows the quantification of internal model deformation using DVC. The continuous improvement of DVC algorithms warrants the re-analysis of already available XRCT data sets allowing new insights in the spatial and temporal characteristics of internal model deformation. Our revised DVC workflow highlights the importance of carefully preprocessing the XRCT data to ensure cubic voxels, multi-pass DVC, postprocessing and the use of strain quantities appropriate for large time increments between subsequent XRCT scans. Applied on XRCT imagery from the model presented in *Zwaan et al.* (2018), our workflow provides new insights into the general evolution of model internal deformation by means of finite stretch and rotation. The demonstrated workflow represents a further advance in the analysis of analogue experiments and can also be applied to XRCT-scanned models studying other tectonic regimes.

Our new DVC results are in general in agreement with those from *Zwaan et al.* (2018), but the new workflow and the use of map view imagery provide a much-improved picture of model internal deformation. Overall, our DVC analysis depicts a clear distinction between deformation in the brittle and viscous layers; faulting and rift segment interaction

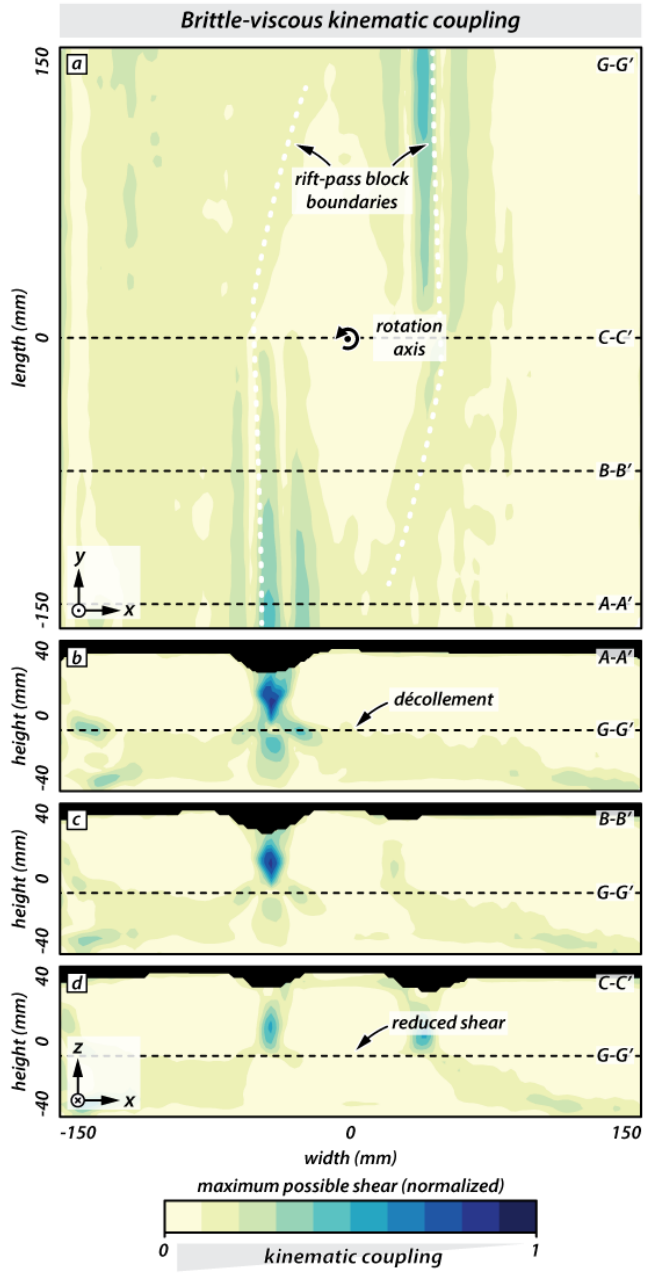

Figure 9 – Brittle-viscous kinematic coupling at the brittle-ductile interface indicated by the normalized maximum possible shear γ_{max}. **a)** Horizontal slice G-G'. Different magnitudes of maximum possible shear in the brittle and viscous layers indicate increased mechanical decoupling at the brittle-viscous interface between the two model domains. White dashed lines indicate the confinement of the rift-pass block by the two rift segments. **b)** Model transect A-A' displays enhanced decoupling below the rift-pass block where a décollement forms indicated by enhanced shear. **c)** Transect B-B' is characterized by decreasing shear below the rift-pass block. **d)** At the central model transect C-C', the décollement below the rift-pass block vanishes due to low shear values between the brittle and viscous model layers.

in the brittle layer causes apparent quasi-rigid body rotation (i.e., the rotation of the rift-pass block about a vertical axis; Figure 7) that gradually decreases in the viscous layer (Figure 8). The interaction between the brittle and viscous layers is documented in Figure 9 describing kinematic brittle-viscous coupling by means of γ_{max}. Spatial variations of γ_{max} further imply that motions in the brittle and viscous layer influence each other. Presumably, the rift-pass block rotation also affects the occurrence and magnitude of flow in the viscous layer which we discuss below.

4.1 DVC Analysis in Other Analogue Modelling Studies and Novelty of our Work

Adam et al. (2013) were the first to successfully apply DVC on consecutive XRCT volume sets of analogue models to fully quantify 3D deformation and the kinematic evolution of a pop-up structure within a fold and thrust belt. Their extensive analysis of XRCT data preprocessing resulted in an optimized vector resolution of 2.5 mm and an accuracy of ±0.04 mm. By contrast, the vector resolution in *Zwaan et al.* (2018) is reduced by a factor ~2 (i.e., 4.8 mm vector resolution) with an accuracy of ±0.06 mm. This apparent step backwards in vector resolution is due to the considerably different model setups and dimensions between both studies. The analogue models from *Adam et al.* (2013) consisted of a brittle-only setup to simulate upper crustal shortening with a 3 cm quartz sand layer and a total model length and width of 30 cm and 20 cm, respectively. These models were placed in the XRCT scanner in such a way, that the width of the model within the XRCT plane was constant throughout the experiment.

By contrast, the models from *Zwaan et al.* (2018) include a 4 cm thick quartz sand layer on top of a 4 cm thick viscous mixture with a total model width of 30.5 cm (see Figure 2b) that increased during the experiment run to a total width of 33.5 cm. Hence, the chosen XRCT scan window size (Figure 2c) is substantially larger for XRCT scanned models in *Zwaan et al.* (2018), with the XRCT plane matrix resolution of 512 by 512 eventually leading to a coarser absolute voxel resolution in *Zwaan et al.* (2018). Additionally, attenuation of X-rays is also dependent on the thickness and width (and resulting aspect ratio) of the material within the XRCT plane (*Colletta et al.*, 1991), leading to a better XRCT image quality for the models in *Adam et al.* (2013). Moreover, preprocessing in *Adam et al.* (2013) was optimized for one specific material (i.e., quartz sand) with constant density, whereas the choice of scan parameters in *Zwaan et al.* (2018) had to take into account two different model materials with different X-ray attenuation values (*Colletta et al.*, 1991). In that light, DVC results in *Zwaan et al.* (2018) represent a major improvement since the authors were able to apply DVC on a two-layer brittle-viscous model with both domains depicting different deformation styles.

Poppe et al. (2019) used a wide-beam XRCT scanner allowing continuous scanning of a stationary model box to simulate fluid propagation (i.e., magma intrusion) into a granular host material. Unlike

the large-scale tectonic models from *Adam et al.* (2013) and *Zwaan et al.* (2018), the internal driving force for deformation in their models cannot be halted once initiated. Therefore, helical scans (i.e., simultaneous scanning by a rotating X-ray beam while the sample is moved through the XRCT scanner) in standard medical XRCT scanners somewhat limit their application to analogue models where deformation is applied externally and can be interrupted during scan procedures. Furthermore, *Poppe et al.* (2019) combined the model internal quantification using DVC with the topographic evolution by extracting the model surface from XRCT volumes and investigated how magma intrusion affects the topographic evolution.

Similarly, *Schmid et al.* (2022) used DVC applied on XRCT volumes to investigate lower crustal flow in rotational rifting and its effect on topography. However, they combined DVC with high-resolution 3D stereo DIC applied to the model surface to quantify near-surface strain resulting from deep-seated viscous flow. *Schmid et al.* (2022) obtained volumetric data sets from standard medical XRCT scans, following the procedures of *Adam et al.* (2013) and *Zwaan et al.* (2018), so that vector resolution and accuracy were in the same order as in this study. However, the DVC analysis completed by *Schmid et al.* (2022) was limited to displacement components as attenuation artefacts occurred along the boundaries of the experimental apparatus, preventing accurate strain analysis.

The new work presented in this paper builds on the gradual advances of the aforementioned studies (e.g., XRCT data preprocessing, DVC applied to brittle-viscous models) and extends a general DVC workflow using finite stretches and rotation to gain new insights into model internal deformation.

4.2 Interaction of Block Rotation and Lower Crustal Flow

Two end-member scenarios for rigid-block rotations have been described previously; the edge-driven (or pinned block) model and the floating block model (*McKenzie and Jackson*, 1983, 1986; *Schouten et al.*, 1993).

In the edge-driven model (Figure 1a), rigid blocks rotate driven by interactions on their lateral margins (i.e., plate boundaries) where considerable resistance occurs (*Schouten et al.*, 1993). The interaction between the rotating block and its lateral margins exerts a drag on the underlying viscous flow that perturbs the regional flow locally (*Lachenbruch and Sass*, 1992; *Lamb*, 1994). Applied to nature, this implies the presence of a horizontal transitional layer between the brittle upper crust and the underlying ductile lower crust, that shows enhanced horizontal shearing and determines the degree to which motions at depth are coupled to near-surface movements (*Lamb*, 1994; *Thatcher*, 1995).

We document such a transitional layer at the brittle-viscous interface in our model analysis, where enhanced shearing occurs (Figure 9). This suggests, that displacement components in the two model layers depict different directions and magnitudes leading to a shear horizon at the brittle-viscous interface (Figure 9). Undeniably, vertical flow near the viscous seeds as well as subsidence within the rift segments largely contribute to the maximum λ_{max} values observed in those areas (Figures 5g-l, 6g-l), whereas outside the rift segments λ_{max} values are dominated by the horizontal components u_x and u_y (Figures 5a-f, 6a-f). In the latter case, depth profiles of λ_{max} depict a clear jump in shearing at the brittle-viscous interface (Figure 10). Within the rift-pass block, the increase of λ_{max} over time is minor and evenly distributed throughout the brittle layer, confirming that the rift-pass block moves en masse. In contrast, the viscous layer depicts a gradual increase of λ_{max} over time but, more importantly, also shows spatial variation of λ_{max} from the outer part of the model (depth profile at A-A'; Figure 10a) towards the rotation axis (depth profile at C-C'; Figure 10c).

The floating block model (Figure 1b) describes block rotation due to a deforming continuum below the brittle upper crust where shear may occur internally within the viscous domain but is negligible on the lateral margins of the rift-pass block (*Jackson and Molnar*, 1990). Considerations for the floating block model in *McKenzie and Jackson* (1983) are purely theoretical and based on a simple kinematic 2D model where a velocity field with constant gradients occurs between a fixed plate and a moving plate with constant velocities. However, the model has been proven valuable for explaining palaeomagnetic declination rotations.

Even though early deformation stages in our model analysis are accompanied by minor viscous flow below the viscous seeds (with an opposite direction compared to rift propagation; *Zwaan et al.*, 2018), we can exclude the floating block model as the driving mechanism of rotation in our experiment. Due to the zero y-velocity boundary conditions, no regional flow pattern occurs that can lead to a floating block outcome. Moreover, when regional-scale flow patterns in the underlying substratum drive rotation of the brittle block on top, displacement rates should be identical in both layers of the floating block model (*Lamb*, 1994). In our model analysis, R_z in the viscous layer is lower than in the brittle one at any time. The same holds for incremental rotations, where elevated rotations in the viscous layer would hint at transient stages, when the floating-block end-member is favored. In our case, the u_y flow pattern in the viscous model layer is a consequence of the rotating rift-pass block exerting a drag force on the viscous substratum.

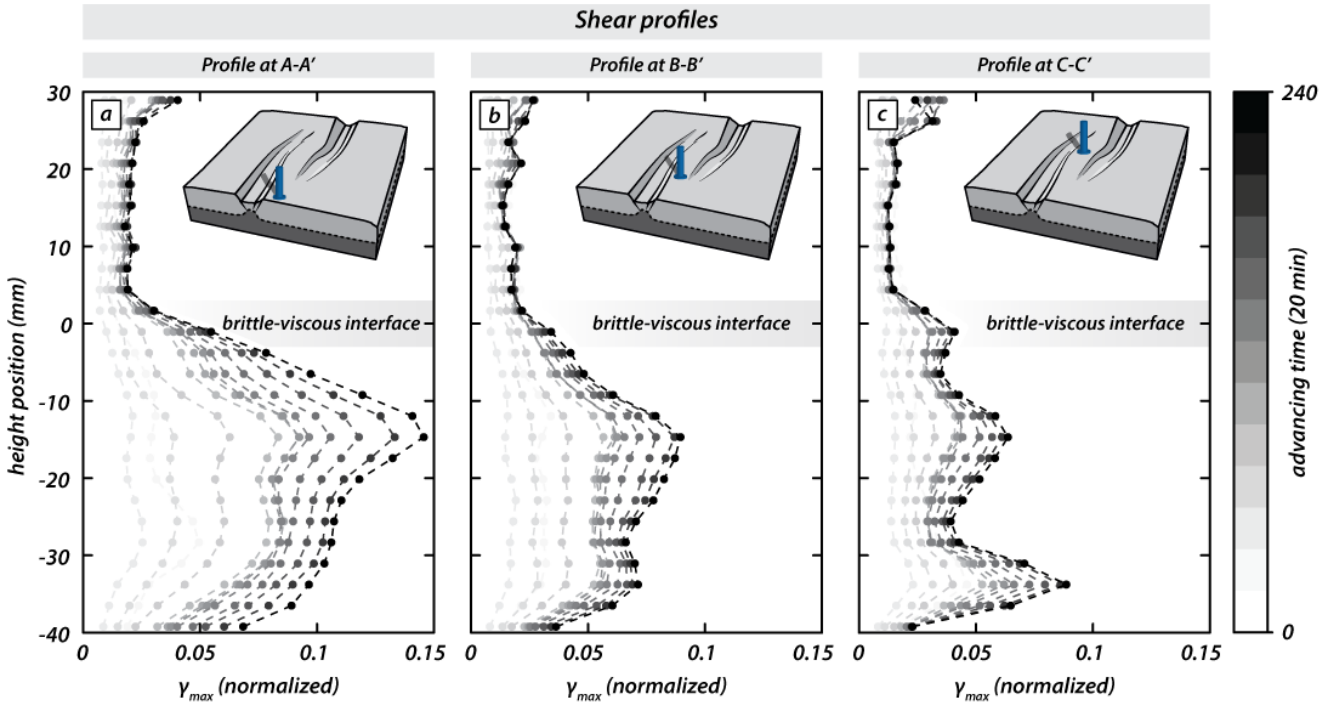

Figure 10 – Profiles and evolution of the maximum possible shear γ_{max} at rift transects A-A', B-B', and C-C'. **a-c)** Depth profiles indicating increased shear values with increasing distance from the rotation axis. Gray scales of the lines refer to the respective time step (in 20 min increments). Blue poles in insets refer to the position of the profiles. Shearing increases with increasing distance to the rotation axis resulting in the most prominent shear horizon at the rift-transect C-C' (see text for details). Maximum possible shear values are normalized within the range [0, 1] (see also Figure 7).

In this light, horizontal shearing at the brittle-viscous transition favors the edge-driven model as a viable mechanism for the rift-pass block rotation about a vertical axis (Figure 7) in our presented analogue model. The resistance along the rift segments allows for higher rotation rates compared to the floating block model (see Figure 2 in *Schouten et al.*, 1993) and consequently, relative motions (hence, rotations; Figures 7, 8) between brittle and viscous model layers; resulting shear at the brittle-viscous interface indicates relatively low kinematic coupling between the two model layers (Figures 9, 10). However, spatial variations of coupling near the brittle-viscous interface occur: Quasi-rigid body rotation in the brittle layer causes increasing horizontal displacements further away from the rotation axis, that lead to higher shear values compared to those in the vicinity of the rotation axis (Figures 9, 10).

Although originally proposed for rotating oceanic microplates, the edge-driven model best matches our experimental observations, which are also in agreement with a previous numerical study by *Glerum et al.* (2020) on the rotation of the Victoria plate in East Africa, in which the authors propose edge-driven rotation for continental microplates.

4.3 Rift-pass Block Rotation and Concomitant Rift-axis-parallel Flow

Our findings suggest an edge-driven rift-pass block evolution as follows (Figure 11a): In an early phase (left panel), rigid-block rotation in the brittle model layer is driven by the initial geometry of the rift segments that exert a drag force on the central model domain as rift segments develop and laterally propagate. This first phase is accompanied by minor flow below the viscous seeds with an opposite direction compared to rift propagation, which has also been proposed in *Zwaan et al.* (2018). In a second phase (middle panel), rotation in the brittle layer enhances viscous out-of-plane flow documented by enhanced horizontal shearing at the brittle-viscous interface below the rift-pass block (Figure 9). Simultaneously, viscous material near the seeds flows upwards (compensating for brittle thinning above) and widens, which results in enhanced flow below the viscous seeds. With progressive rotation of the rift-pass block (right panel), viscous out-of-plane flow increases within the entire viscous model layer. This rotation-induced out-of-plane flow (i.e., u_y; Figures 5d-f, 6d-f) in the viscous layer is relatively strong compared to u_y in the brittle layer and additionally contributes to shear at the brittle-viscous interface. resulting in increased shearing at the brittle-viscous interface.

Rift-axis parallel lower-crustal flow also occurs in natural rift-pass structures and may transport a substantial amount of lower crustal material out of a 2D section plane resulting in overestimation of crustal extension in rift sections (*Clift*, 2015). The effect of rift-axis parallel flow thus clearly must be considered when estimating crustal extension from rift-perpendicular cross sections in natural rifts.

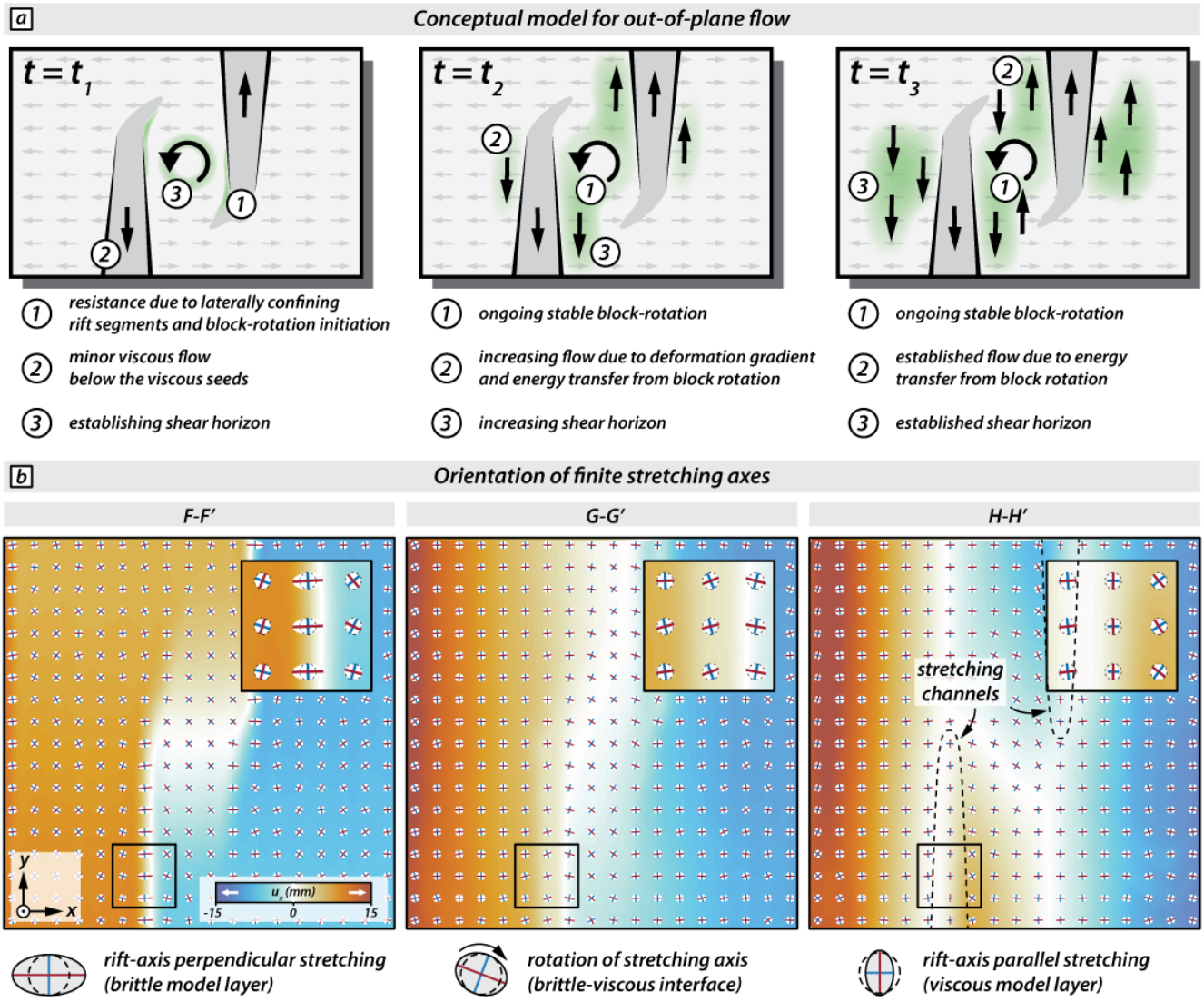

Figure 11 – Conceptual model for rift-axis parallel flow and stretching in the viscous model layer. **a)** Conceptual model of edge-driven rotation of the rift-pass block in the upper brittle model layer and increasing lower crustal flow (see text for details). Black arrows refer to the increasing out-of-plane flow component (i.e., u_y displacement component). Light grey arrows refer to the u_x displacement field parallel to the direction of extension. **b)** Orientation of finite stretching axes. Increasing u_y flow in the viscous layer over time causes rotation of the finite stretching axes from a rift-axis perpendicular, to a rift-axis parallel direction from the brittle (F-F') to the viscous (H-H') model layer, respectively (see text for details). Insets refer to the finite stretching axes in areas indicated by black squares. Black dashed lines indicate channels below the viscous seed, where rift-axis parallel stretching occurs. Maps in the background show the u_x displacement component.

Moreover, such flow would imply, that lower crustal rocks show rift-axis parallel stretching, as a result of rift-axis perpendicular extension in the upper brittle crust. This has recently been proposed, for example, in the South China Sea (*Clift*, 2015), the Woodlark Rift (*Little et al.*, 2007, 2011, 2013), the Ruby Mountains, Nevada (*MacCready et al.*, 1997), and the Nigde Massif, Turkey (*Gautier et al.*, 2008), where rift-axis parallel regional flow may be the response to a divergence-velocity gradient along the rift axis. *Schmid et al.* (2022) document rift-axis parallel flow in analogue models with an applied divergence velocity gradient but remain speculative as to whether such flow is strong enough to cause rift-axis parallel stretching.

DVC analysis of the model presented here implies that such rift-axis parallel lower crustal flow may also occur due to propagating and interacting rift segments in an orthogonal rift setting without the need of a divergence velocity gradient. If such flow is strong enough (compared to the rift-axis perpendicular deformation), it will cause a rotation of the stretching direction away from rift-axis perpendicular to parallel. Consequently, rift-axis parallel lower crustal stretching occurs concomitant with rift-perpendicular brittle upper crustal stretching. Indeed, our analysis shows this rotation of the finite stretching axis (Figure 11b) within channels below the viscous seeds and suggests that such rift-axis parallel stretching of the lower crust may also occur in natural settings.

5 Conclusion

We present a new DVC workflow that entails improved XRCT data preprocessing, higher vector resolution (compared to previous studies) using overlapping sub-voxels, and enhanced postprocessing for visualizing finite stretch and quasi-rigid body rotation. Using this workflow, we re-analyzed XRCT data from a brittle-viscous two-layer analogue rifting model originally presented in *Zwaan et al.* (2018) and show the quantitative evolution of a rift-pass structure in vertical and horizontal slices through the brittle and viscous model layers and near the brittle-viscous interface. This approach presents novel insights into the initiation and evolution of rift-pass block rotation. Our main findings:

1. The improved workflow considers cubic voxels, necessary for the DVC analysis and allows for a novel quantitative investigation of block rotation and kinematic coupling between brittle and viscous model layers. This highlights the importance of revisiting existing volumetric data sets of analogue modelling studies.
2. Polar decomposition of the deformation gradient tensor enables quantitative documentation of the evolution of the rift-pass structure in the brittle layer and its effect on deformation in the viscous layer. While shear and rotation in the brittle layer depict well-defined zones, rotation gradually decreases in the viscous layer while shear is prevalent throughout.
3. Shear at the brittle-viscous interface documents different degrees of kinematic brittle-viscous coupling that vary temporally and spatially within the rift-pass structure.
4. The rift-pass block in the brittle layer rotates about a vertical axis due to lateral resistance along the rift segments (edge-driven model) that exerts a drag force on the underlying viscous layer. There, flow is disturbed, resulting in prominent out-of-plane flow and rift-axis parallel stretch of the viscous layer below the viscous seeds.
5. In nature, the degree of kinematic coupling between upper crustal faulting and lower crustal ductile flow is generally difficult to establish. However, our model analysis suggests that edge-driven rift-pass block rotation locally weakens kinematic coupling and results in rift-axis parallel flow in the lower crust. Such flow may transport considerable amounts of material out of a rift-perpendicular 2D plane, which must be considered when estimating crustal extension.

Acknowledgements

We would like to thank Taco Broerse for constructive discussions regarding the proper use of strain tensors. Kirsten Elger and Florian Ott helped in creating the GFZ Data publication containing the supplementary material (*Schmid et al.*, 2024). We thank Jacqueline Reber, Taco Broerse, editor Janine Kavanagh, and topical editor Leonardo Pichel for their detailed and constructive comments, which significantly helped to improve this paper.

This research was supported by the Swiss National Science Foundation [grant numbers 200021_147046/1 and 200021_178731] awarded to Guido Schreurs (https://data.snf.ch/grants/grant/178731). Frank Zwaan was further supported by a GFZ Discovery Fund fellowship.

Author contributions

Timothy C. Schmid: Conceptualization, Methodology, Investigation, Formal Analysis, Writing – original draft, Visualization, Data curation. **Jürgen Adam**: Conceptualization, Writing – review & editing, Methodology, Supervision. **Frank Zwaan**: Conceptualization, Investigation, Writing – review & editing. **Guido Schreurs**: Conceptualization, Writing – review & editing, Supervision, Project administration, Funding acquisition, Resources. **Dave Hollis**: Writing – review & editing, Methodology

Data availability

An additional open access data publication on the GFZ Data Service (*Schmid et al.*, 2024) provides additional scripts for data processing and analysis. Links to these datasets are provided in the reference list.

Competing interests

The authors declare no competing interests.

Peer review

This publication was peer-reviewed by Jacqueline Reber and Taco Broerse. The full peer-review report can be found here: tektonika.online/index.php/home/article/view/24/112.

Copyright notice

References

Acocella, Faccenna, Funiciello, and Rossetti (1999), Sand-box modelling of basement-controlled transfer zones in extensional domains, *Terra nova*, *11*(4), 149–156, doi: 10.1046/j.1365-3121.1999.00238.x.

Acocella, V. (2008), Transform faults or Overlapping Spreading Centers? Oceanic ridge interactions revealed by analogue models, *Earth and planetary science letters*, *265*(3-4), 379–385, doi: 10.1016/j.epsl.2007.10.025.

Adam, J., J. L. Urai, B. Wieneke, O. Oncken, K. Pfeiffer, N. Kukowski, J. Lohrmann, S. Hoth, W. van der Zee, and J. Schmatz (2005), Shear localisation and strain distribution during tectonic faulting—new insights from granular-flow experiments and high-resolution optical image correlation techniques, *Journal of structural geology*, *27*(2), 283–301, doi: 10.1016/j.jsg.2004.08.008.

Adam, J., M. Klinkmüller, G. Schreurs, and B. Wieneke (2013), Quantitative 3D strain analysis in analogue experiments simulating tectonic deformation: Integration of X-ray computed tomography and digital volume correlation techniques, *Journal of structural geology*, *55*, 127–149, doi: 10.1016/j.jsg.2013.07.011.

Allken, V., R. S. Huismans, and C. Thieulot (2011), Three-dimensional numerical modeling of upper crustal extensional systems, *Journal of geophysical research*, *116*(B10), doi: 10.1029/2011jb008319.

Allken, V., R. S. Huismans, and C. Thieulot (2012), Factors controlling the mode of rift interaction in brittle-ductile coupled systems: A 3D numerical study, *Geochemistry, geophysics, geosystems: G(3)*, *13*(5), doi: 10.1029/2012gc004077.

Allmendinger, R. W., N. Cardozo, and D. M. Fisher (2011), *Structural geology algorithms: Vectors and tensors*, Cambridge University Press, Cambridge, England.

Amidror, I. (2002), Scattered data interpolation methods for electronic imaging systems: a survey, *Journal of electronic imaging*, *11*(2), 157, doi: 10.1117/1.1455013.

Axen, G. J., J. Selverstone, T. Byrne, and J. M. Fletcher (1998), If the strong crust leads, will the weak crust follow, *GSA today: a publication of the Geological Society of America*, *8*(12), 1–8.

Bosworth, W. (1985), Geometry of propagating continental rifts, *Nature*, *316*(6029), 625–627, doi: 10.1038/316625a0.

Boutelier, D. (2016), TecPIV—A MATLAB-based application for PIV-analysis of experimental tectonics, *Computers & geosciences*, *89*, 186–199, doi: 10.1016/j.cageo.2016.02.002.

Boutelier, D., C. Schrank, and K. Regenauer-Lieb (2019), 2-D finite displacements and strain from particle imaging velocimetry (PIV) analysis of tectonic analogue models with TecPIV, *Solid earth*, *10*(4), 1123–1139, doi: 10.5194/se-10-1123-2019.

Broerse, T., N. Krstekanić, C. Kasbergen, and E. Willingshofer (2021), Mapping and classifying large deformation from digital imagery: application to analogue models of lithosphere deformation, *Geophysical journal international*, *226*(2), 984–1017, doi: 10.1093/gji/ggab120.

Brun, J.-P. (1999), Narrow rifts versus wide rifts: inferences for the mechanics of rifting from laboratory experiments, *Philosophical transactions. Series A, Mathematical, physical, and engineering sciences*, *357*(1753), 695–712, doi: 10.1098/rsta.1999.0349.

Brune, S., G. Corti, and G. Ranalli (2017), Controls of inherited lithospheric heterogeneity on rift linkage: Numerical and analog models of interaction between the Kenyan and Ethiopian rifts across the Turkana depression: Rift Linkage Modeling, Turkana Region, *Tectonics*, *36*(9), 1767–1786, doi: 10.1002/2017tc004739.

Buck, W. R. (1991), Modes of continental lithospheric extension, *Journal of geophysical research*, *96*(B12), 20,161–20,178, doi: 10.1029/91jb01485.

Buiter, S. J. H., R. S. Huismans, and C. Beaumont (2008), Dissipation analysis as a guide to mode selection during crustal extension and implications for the styles of sedimentary basins, *Journal of geophysical research*, *113*(B6), doi: 10.1029/2007JB005272.

Bürgmann, R., and G. Dresen (2008), Rheology of the lower crust and upper mantle: Evidence from rock mechanics, geodesy, and field observations, *Annual review of earth and planetary sciences*, *36*(1), 531–567, doi: 10.1146/annurev.earth.36.031207.124326.

Chaipornkaew, L., H. Elston, M. Cooke, T. Mukerji, and S. A. Graham (2022), Predicting off-fault deformation from experimental strike-slip fault images using convolutional neural networks, *Geophysical research letters*, *49*(2), e2021GL096,854, doi: 10.1029/2021gl096854.

Clift, P. (2015), Coupled onshore erosion and offshore sediment loading as causes of lower crust flow on the margins of South China Sea, *Geoscience letters*, *2*(1), 1–11, doi: 10.1186/s40562-015-0029-9.

Collanega, L., C. A.-L. Jackson, R. E. Bell, A. J. Coleman, A. Lenhart, and A. Breda (2018), How do intra-basement fabrics influence normal fault growth? Insights from the Taranaki Basin, offshore New Zealand, *EarthArXiv*.

Colletta, B., J. Letouzey, R. Pinedo, J. F. Ballard, and P. Balé (1991), Computerized X-ray tomography analysis of sandbox models: Examples of thin-skinned thrust systems, *Geology*, *19*(11), 1063, doi: 10.1130/0091-7613(1991)019<1063:cxrtao>2.3.co;2.

D'Errico, J. (2008), Inpainting nan elements in 3-d, *MATLAB Central File Exchange*.

Diebel, J. (2006), Representing attitude : Euler angles , unit quaternions , and rotation vectors, *Matrix*, *58*(15-16), 1–35.

Dooley, T. P., M. P. A. Jackson, and M. R. Hudec (2009), Inflation and deflation of deeply buried salt stocks during lateral shortening, *Journal of structural geology*, *31*(6), 582–600, doi: 10.1016/j.jsg.2009.03.013.

Fossen, H., R. Schultz, E. Rundhovde, A. Rotevatn, and S. Buckley (2010), Fault linkage and graben stepovers in the Canyonlands (Utah) and the North Sea Viking Graben, with implications for hydrocarbon migration and accumulation, *AAPG Bulletin*, *94*(5), 597–613, doi: 10.1306/10130909088.

Gautier, P., E. Bozkurt, V. Bosse, E. Hallot, and K. Dirik (2008), Coeval extensional shearing and lateral underflow during Late Cretaceous core complex development in the Niğde Massif, Central Anatolia, Turkey: CORE COMPLEX IN CENTRAL ANATOLIA, *Tectonics*, *27*(1), doi: 10.1029/2006tc002089.

Gawthorpe, R. L., and J. M. Hurst (1993), Transfer zones in extensional basins: their structural style and influence on drainage development and stratigraphy, *Journal of the Geological Society*, *150*(6), 1137–1152, doi: 10.1144/gsjgs.150.6.1137.

Giorgis, S., M. Markley, and B. Tikoff (2004), Vertical-axis

rotation of rigid crustal blocks driven by mantle flow, *Geological Society special publication*, *227*(1), 100–183, doi: 10.1144/GSL.SP.2004.227.01.05.

Glerum, A., S. Brune, D. S. Stamps, and M. R. Strecker (2020), Victoria continental microplate dynamics controlled by the lithospheric strength distribution of the East African Rift, *Nature communications*, *11*(1), 2881, doi: 10.1038/s41467-020-16176-x.

Heilman, E., F. Kolawole, E. A. Atekwana, and M. Mayle (2019), Controls of basement fabric on the linkage of rift segments, *Tectonics*, *38*(4), 1337–1366, doi: 10.1029/2018tc005362.

Hounsfield, G. (1973), Computerized transverse axial scanning (tomography): Part I. Description of system. 1973, *The British journal of radiology*, *68*(815), H166–72, doi: 10.1259/0007-1285-46-552-1016.

Jackson, J., and P. Molnar (1990), Active faulting and block rotations in the Western Transverse Ranges, California, *Journal of geophysical research*, *95*(B13), 22,073–22,087, doi: 10.1029/jb095ib13p22073.

Jackson, J., J. Haines, and W. Holt (1992), The horizontal velocity field in the deforming Aegean Sea region determined from the moment tensors of earthquakes, *Journal of geophysical research*, *97*(B12), 17,657–17,684, doi: 10.1029/92jb01585.

Koehn, D., K. Aanyu, S. Haines, and T. Sachau (2008), Rift nucleation, rift propagation and the creation of basement micro-plates within active rifts, *Tectonophysics*, *458*(1-4), 105–116, doi: 10.1016/j.tecto.2007.10.003.

Kolawole, F., E. A. Atekwana, D. A. Laó-Dávila, M. G. Abdelsalam, P. R. Chindandali, J. Salima, and L. Kalindekafe (2018), Active deformation of Malawi rift's North Basin hinge zone modulated by reactivation of preexisting Precambrian shear zone fabric, *Tectonics*, *37*(3), 683–704, doi: 10.1002/2017tc004628.

Lachenbruch, A. H., and J. H. Sass (1992), Heat flow from Cajon Pass, fault strength, and tectonic implications, *Journal of geophysical research*, *97*(B4), 4995–5015, doi: 10.1029/91jb01506.

Lamb, S. H. (1994), Behavior of the brittle crust in wide plate boundary zones, *Journal of geophysical research*, *99*(B3), 4457–4483, doi: 10.1029/93jb02574.

Le Calvez, J. H., and B. C. Vendeville (2002), Physical modeling of normal faults and Graben relays above salt: A qualitative and quantitative analysis, *Gulf Coast Association of Geological Societies Transactions*, *52*, 599–606.

Little, T. A., S. L. Baldwin, P. G. Fitzgerald, and B. Monteleone (2007), Continental rifting and metamorphic core complex formation ahead of the Woodlark spreading ridge, D'Entrecasteaux Islands, Papua New Guinea: METAMORPHIC CORE COMPLEX, WOODLARK RIFT, *Tectonics*, *26*(1), doi: 10.1029/2005tc001911.

Little, T. A., B. R. Hacker, S. M. Gordon, S. L. Baldwin, P. G. Fitzgerald, S. Ellis, and M. Korchinski (2011), Diapiric exhumation of Earth's youngest (UHP) eclogites in the gneiss domes of the D'Entrecasteaux Islands, Papua New Guinea, *Tectonophysics*, *510*(1-2), 39–68, doi: 10.1016/j.tecto.2011.06.006.

Little, T. A., B. R. Hacker, S. J. Brownlee, and G. Seward (2013), Microstructures and quartz lattice-preferred orientations in the eclogite-bearing migmatitic gneisses of the D'Entrecasteaux Islands, Papua New Guinea: MICROSTRUCTURES, LPOS OF UHP ROCKS, PNG, *Geochemistry, geophysics, geosystems: G(3)*, *14*(6), 2030–2062, doi: 10.1002/ggge.20132.

MacCready, T., A. W. Snoke, J. E. Wright, and K. A. Howard (1997), Mid-crustal flow during Tertiary extension in the Ruby Mountains core complex, Nevada, *Geological Society of America bulletin*, *109*(12), 1576–1594, doi: 10.1130/0016-7606(1997)109<1576:mcfdte>2.3.co;2.

Malvern, L. E. (1969), *Introduction to the mechanics of a continuous medium*, Prentice-Hall Series in Engineering of the Physical Sciences, Prentice Hall, Philadelphia, PA.

Mandl, G. (1988), *Mechanics of tectonic faulting: Models and basic concepts*, Elsevier Publishing Company.

Mareschal, J.-C., and C. Jaupart (2013), Radiogenic heat production, thermal regime and evolution of continental crust, *Tectonophysics*, *609*, 524–534, doi: 10.1016/j.tecto.2012.12.001.

Martin, A. K. (1984), Propagating rifts: Crustal extension during continental rifting, *Tectonics*, *3*(6), 611–617, doi: 10.1029/tc003i006p00611.

McKenzie, D., and J. Jackson (1983), The relationship between strain rates, crustal thickening, palaeomagnetism, finite strain and fault movements within a deforming zone, *Earth and planetary science letters*, *65*(1), 182–202, doi: 10.1016/0012-821x(83)90198-x.

McKenzie, D., and J. Jackson (1986), A block model of distributed deformation by faulting, *Journal of the Geological Society*, *143*(2), 349–353, doi: 10.1144/gsjgs.143.2.0349.

Morley, C., R. Nelson, T. L. Patton, and S. Munn (1990), Transfer zones in the East African rift system and their relevance to hydrocarbon exploration in rifts (1), *AAPG Bulletin*, *74*(8), 1234–1253, doi: 10.1306/0C9B2475-1710-11D7-8645000102C1865D.

Nelson, R., T. L. Patton, and C. Morley (1992), Rift-segment interaction and its relation to hydrocarbon exploration in continental rift systems (1), *AAPG Bulletin*, *76*(8), 1153–1169, doi: 10.1306/BDFF898E-1718-11D7-8645000102C1865D.

Oldenburg, D. W., and J. N. Brune (1975), An explanation for the orthogonality of ocean ridges and transform faults, *Journal of geophysical research*, *80*(17), 2575–2585, doi: 10.1029/jb080i017p02575.

Panien, M., S. Buiter, G. Schreurs, and O. Pfiffner (2006), Inversion of a symmetric basin: insights from a comparison between analogue and numerical experiments, *Geological Society special publication*, *253*(1), 253–270, doi: 10.1144/GSL.SP.2006.253.01.13.

Paul, D., and S. Mitra (2012), Experimental models of transfer zones in rift systems, *AAPG Bulletin*, *97*(5), 759–780, doi: 10.1306/10161212105.

Pollard, D. D., and A. Aydin (1984), Propagation and linkage of oceanic ridge segments, *Journal of geophysical research*, *89*(B12), 10,017–10,028, doi: 10.1029/jb089ib12p10017.

Poppe, S., E. P. Holohan, O. Galland, N. Buls, G. Van Gompel, B. Keelson, P.-Y. Tournigand, J. Brancart, D. Hollis, A. Nila, and M. Kervyn (2019), An inside perspective on magma intrusion: Quantifying 3D displacement and strain in laboratory experiments by dynamic X-ray computed tomography, *Frontiers in earth science*, *7*, 62, doi: 10.3389/feart.2019.00062.

Raffel, M., C. E. Willert, F. Scarano, C. J. Kähler, S. T.

Wereley, and J. Kompenhans (2018), Post-processing of PIV Data, in *Particle Image Velocimetry*, pp. 243–283, Springer International Publishing, Cham, doi: 10.1007/978-3-319-68852-7_7.

Rosendahl, B. (1987), Architecture of continental rifts with special reference to east Africa, *Annual review of earth and planetary sciences*, *15*(1), 445–503, doi: 10.1146/annurev.earth.15.1.445.

Schellart, W. P., M. W. Jessell, and G. S. Lister (2003), Asymmetric deformation in the backarc region of the Kuril arc, northwest Pacific: New insights from analogue modeling: ASYMMETRIC BACKARC DEFORMATION BEHIND THE KURIL ARC, *Tectonics*, *22*(5), doi: 10.1029/2002tc001473.

Schmid, T., G. Schreurs, and J. Adam (2022), Rotational extension promotes coeval upper crustal brittle faulting and deep-seated rift-axis parallel flow: Dynamic coupling processes inferred from analog model experiments, *Journal of Geophysical Research, [Solid Earth]*, *127*, e2022JB024,434, doi: 10.1029/2022JB024434.

Schmid, T. C., J. Adam, F. Zwaan, G. Schreurs, D. Hollis, and M. Rosenau (2024), Digital Volume Correlation (DVC) data from an analogue experiment exploring kinematic coupling of brittle and viscous deformation, *GFZ Data Services*, doi: 10.5880/fidgeo.2024.028.

Schouten, H., K. D. Klitgord, and D. G. Gallo (1993), Edge-driven microplate kinematics, *Journal of geophysical research*, *98*(B4), 6689–6701, doi: 10.1029/92jb02749.

Schreurs, G., and B. Colletta (1998), Analogue modelling of faulting in zones of continental transpression and transtension, *Geological Society special publication*, *135*(1), 59–79, doi: 10.1144/GSL.SP.1998.135.01.05.

Schreurs, G., R. Hänni, and P. Vock (2002), Analogue modelling of transfer zones in fold-and-thrust belts: a 4-D analysis, *Journal of the virtual explorer*, *07*, 67–73, doi: 10.3809/jvirtex.2002.00047.

Schreurs, G., R. Hänni, M. Panien, and P. Vock (2003), Analysis of analogue models by helical X-ray computed tomography, *Geological Society special publication*, *215*(1), 213–223, doi: 10.1144/GSL.SP.2003.215.01.20.

Schueller, S., F. Gueydan, and P. Davy (2010), Mechanics of the transition from localized to distributed fracturing in layered brittle–ductile systems, *Tectonophysics*, *484*(1-4), 48–59, doi: 10.1016/j.tecto.2009.09.008.

Tentler, T., and V. Acocella (2010), How does the initial configuration of oceanic ridge segments affect their interaction? Insights from analogue models, *Journal of geophysical research*, *115*(B1), doi: 10.1029/2008jb006269.

Thatcher, W. (1995), Microplate versus continuum descriptions of active tectonic deformation, *Journal of geophysical research*, *100*(B3), 3885–3894, doi: 10.1029/94jb03064.

Thielicke, W. (2014), The flapping flight of birds: Analysis and application, Ph.D. thesis, University of Groningen, The Netherlands.

Thielicke, W., and E. Stamhuis (2014), PIVlab – towards user-friendly, affordable and accurate digital particle image velocimetry in MATLAB, *Journal of open research software*, *2*(1), 30, doi: 10.5334/JORS.BL.

Tikoff, B., C. Teyssier, and C. Waters (2002), Clutch tectonics and the partial attachment of lithospheric layers, *Stephan Mueller special publication series*, *1*, 57–73, doi: 10.5194/smsps-1-57-2002.

Tikoff, B., R. Russo, C. Teyssier, and A. Tommasi (2004), Mantle-driven deformation of orogenic zones and clutch tectonics, *Geological Society special publication*, *227*(1), 41–64, doi: 10.1144/GSL.SP.2004.227.01.03.

Toeneboehn, K., M. L. Cooke, S. P. Bemis, A. M. Fendick, and J. Benowitz (2018), Stereovision combined with particle tracking velocimetry reveals advection and uplift within a restraining bend simulating the Denali fault, *Frontiers in earth science*, *6*, 152, doi: 10.3389/feart.2018.00152.

Westerweel, J., and F. Scarano (2005), Universal outlier detection for PIV data, *Experiments in fluids*, *39*(6), 1096–1100, doi: 10.1007/s00348-005-0016-6.

Wieneke, B. (2015), PIV uncertainty quantification from correlation statistics, *Measurement Science and Technology*, *26*(7), 074,002, doi: 10.1088/0957-0233/26/7/074002.

Wieneke, B. (2017), PIV Uncertainty Quantification and Beyond, Ph.D. thesis, TU Delft, The Netherlands, doi: 10.4233/UUID:4CA8C0B8-0835-47C3-8523-12FC356768F3.

Zwaan, F., and G. Schreurs (2017), How oblique extension and structural inheritance influence rift segment interaction: Insights from 4D analog models, *Interpretation*, *5*(1), SD119–SD138, doi: 10.1190/int-2016-0063.1.

Zwaan, F., and G. Schreurs (2020), Rift segment interaction in orthogonal and rotational extension experiments: Implications for the large-scale development of rift systems, *Journal of structural geology*, *140*(104119), 104,119, doi: 10.1016/j.jsg.2020.104119.

Zwaan, F., and G. Schreurs (2023), The link between Somalian Plate rotation and the East African Rift System: an analogue modelling study, *Solid earth*, *14*(8), 823–845, doi: 10.5194/se-14-823-2023.

Zwaan, F., G. Schreurs, J. Naliboff, and S. J. H. Buiter (2016), Insights into the effects of oblique extension on continental rift interaction from 3D analogue and numerical models, *Tectonophysics*, *693*, 239–260, doi: 10.1016/j.tecto.2016.02.036.

Zwaan, F., G. Schreurs, and J. Adam (2018), Effects of sedimentation on rift segment evolution and rift interaction in orthogonal and oblique extensional settings: Insights from analogue models analysed with 4D X-ray computed tomography and digital volume correlation techniques, *Global and planetary change*, *171*, 110–133, doi: 10.1016/j.gloplacha.2017.11.002.

Zwaan, F., G. Schreurs, and S. J. H. Buiter (2019), A systematic comparison of experimental set-ups for modelling extensional tectonics, *Solid earth*, *10*(4), 1063–1097, doi: 10.5194/se-10-1063-2019.

Zwaan, F., G. Schreurs, and M. Rosenau (2020), Rift propagation in rotational versus orthogonal extension: Insights from 4D analogue models, *Journal of structural geology*, *135*(103946), 103,946, doi: 10.1016/j.jsg.2019.103946.